Interaction of Wnt and SHH gradients synchronizes cell cycle exit and differentiation

Authors:

Ruiqi Li[1,2], Yiqun Jiang[3,4*], Sarah Platt[3*], Kevin A. Peterson[5], Hainan Lam[3], Sarah Van[3], Chae Ho Lim[6], Jonathan Levinsohn[7], Eva-Larue Barber[3], David Wang[8], M. Mark Taketo[9], Yuval Kluger[1,2,10,11], Peggy Myung[2,3,4,11,12]

Affiliations:

[1]Computational Biology & Biomedical Informatics Program, Yale University, New Haven, CT 06520, USA

[2]Department of Pathology, Yale University, New Haven, CT 06520, USA

[3]Department of Dermatology, Yale University, New Haven, CT 06520, USA

[4]Molecular, Cellular and Developmental Biology, Yale University, New Haven, CT 06520, USA

[5]The Jackson Laboratory, Bar Harbor, ME 04609, USA

[6]Ronald O. Perelman Department of Dermatology, and Department of Cell Biology, NYU Grossman School of Medicine, New York, NY, USA

[7]Department of Pediatrics, Children's Hospital of Philadelphia, Philadelphia, PA 19104.

[8]Veterans Administration, Ann Arbor Healthcare System, Ann Arbor, MI, USA

[9]Colon Cancer Project, Graduate School of Medicine, Kyoto University, Sakyo, Kyoto 606-8501, Japan

[10]Applied Mathematics Program, Yale University, New Haven, CT 06511, USA

[11]Yale Cancer Center, New Haven, CT 06520, USA

[12]Yale Stem Cell Center, New Haven, CT 06520, USA

*These authors contributed jointly

Keywords:

Hair follicle, dermal condensate, scRNA-sequencing, Wnt, Hedgehog, skin, dermis

Summary:

How signals coordinate cellular proliferation with differentiation to regulate cell fate transitions is poorly understood. Hair follicle dermal condensates (DCs) emerge in developing skin from an acute cell fate transition in which cell cycle exit and molecular differentiation occur simultaneously. Here, we show that the coincident levels of Wnt and Hedgehog signals synchronize these two processes and when uncoupled, trigger them discordantly, resulting in asynchronous arrest and fuzzy cell fate borders. We use an innovative computational approach to dissect out independent processes from scRNA-sequencing data to show that high Wnt activity alone elicits cell cycle exit through a Hedgehog mediator, Gli3. Furthermore, Hedgehog induces DC genes in a Wnt-dependent manner while cell-autonomously accelerating Wnt activity, effectively synchronizing cell cycle exit with DC gene expression. These results show that the interaction of signal gradients can balance proliferation with differentiation to regulate cell fate transitions, revealing a tunable logic to tissue patterning.

Introduction:

To make functional organs, stem and progenitor cells must precisely coordinate proliferation with differentiation, ensuring that distinct cell types assemble into organized populations of the correct size, location, and relative cell proportions. In many tissues, cell cycle exit is associated with terminal differentiation[1]. In certain scenarios such as in mouse or human embryonic stem cells, G1 phase represents a permissive state in which cells are more responsive to cell type transcription factors that induce differentiation genes [2-4]. Here, cells may asynchronously differentiate upon entering G1/G0 phase, and the signals that regulate cell cycle arrest may be independent of those that induce differentiation. In other scenarios such as during cortical neurogenesis, cell cycle regulators may have a dual function in regulating cell type differentiation such that differentiation occurs synchronously with cell cycle phase[5,6]. During development and regeneration, cells can also progress through intermediate states of differentiation (e.g., transit-amplifying progenitors) before undergoing cell cycle exit and terminal differentiation[7-11]. Here, intermediate states of differentiation are coordinated with proliferation. At the same time, failure to coordinate these events can lead to pathological states such as cancer. Therefore, understanding how these processes are coupled is essential for efforts to promote proper regeneration and to mitigate uncontrolled and autonomous growth.

55 A challenge to examining this question during development or regeneration is that different cell types
56 dynamically undergo a mixture of unique and shared biological processes as they progress along a lineage
57 trajectory. This makes it challenging to accurately delineate the progression of cell states within a lineage and
58 the biological processes that govern transitions between cell states. Knowledge of a cell's past and future cell
59 state has been largely dependent on biased tools that durably label specific cell types or cell states. Live
60 imaging has given the ability to track individual cells over time in the same tissue allowing for real-time analysis
61 of cellular differentiation[12-15]. These tools have been instrumental to our understanding of lineage trajectories
62 and the signals that regulate cell fate decisions. Still, dissecting out the specific mechanisms of how cell
63 proliferation and differentiation are coordinated remains limited by the lack of tools and biomarkers to track
64 dynamic changes in these biological processes and to interrogate them individually, especially when they
65 occur concurrently. With the emergence of single-cell RNA-sequencing (scRNA-seq) technology, the ability to
66 profile molecular differences between cells has provided a useful tool to infer signals that regulate cell type
67 differentiation. Still, cell-based trajectory methods often fail to accurately delineate independent processes
68 when they co-occur in the same group of cells, as they collapse cells into a single pseudotemporal path that
69 mixes their distinct dynamics. Thus, the molecular programs that coordinate tissue growth and cell type
70 patterning remain poorly defined in many tissues and poses a major barrier to efforts aimed at recapitulating
71 organ formation *in vitro* or in adult animals.
72
73 In this study, we examine this question using a defined biological system that represents the first differentiated
74 population in mammalian dermis and heralds the onset of dermal lineage diversification[16-18]. In mouse
75 embryos, the hair follicle dermal condensate (DC) emerges at around E14.0-E14.5 in association with
76 overlying epithelial placodes [19-23]. DCs are clusters of specialized quiescent dermal cells that are essential for
77 hair follicle formation. A major obstacle to delineating the sequence of steps that lead to DC genesis is the fact
78 that DC cells form through an acute cell fate transition with few observable intermediate states to identify and
79 track DC progenitors using conventional methods. To address this issue, we previously used scRNA-seq to
80 infer events and signals that precede DC commitment [24,25]. Combined with *in vivo* lineage tracing, we showed
81 that DC cells are immediate quiescent progeny of a highly proliferative population (*Dkk1*-expressing) that
82 divides over a short time frame before DC gene expression and quiescence. We further showed that dermal

83 Wnt/β-catenin and SHH signaling, together, are required and sufficient to induce DC genesis. In other
84 biological systems (e.g., hair follicle epithelial placode, neural tube), Wnt and SHH signaling antagonize each
85 other[13,26,27]. We showed that in the dermis, they unexpectedly cooperate to induce DC genesis. However, it
86 remains unknown how Wnt and Shh act together intracellularly to coordinate a cell fate transition in which cell
87 cycle exit is tightly coupled with molecular DC differentiation, especially as Wnt and SHH antagonize each
88 other in other systems. As such, the DC system provides a unique opportunity to understand how these two
89 key signals can be differentially combined to regulate diverse cell fate patterns and transitions across tissues.
90
91 One problem is that both Wnt and SHH ligands are secreted from a common epidermal source, resulting in
92 covarying and overlapping Wnt and SHH signaling gradients in which both signals are simultaneously
93 upregulated across the transition. Furthermore, both cell cycle exit and molecular DC differentiation occur
94 synchronously across the pre-DC-to-DC transition, making it difficult to separate them apart and to identify their
95 respective molecular mediators. As neither Wnt nor SHH activation alone is sufficient to induce the transition,
96 we sought an approach to dissect out how these two signals regulate the pre-DC-to-DC transition. Here, we an
97 innovative computational method recently developed specifically to deconvolve co-occurring biological
98 processes from whole-transcriptome scRNA-seq data[28]. In contrast to standard cell trajectory inference
99 methods, GeneTrajectory (GT), identifies parallel gene trajectories, allowing independent biological processes
100 to be resolved. Using this method and genetic models that modulate Wnt or SHH activity, we show that while
101 cell cycle exit and DC gene expression occur concurrently, they are not actually regulated by shared
102 downstream effectors as is the case in other tissues (e.g. neurogenesis). Rather, they are synchronized by the
103 mere coupling of upstream Wnt and SHH co-activation, which when combined, result in a sharp cell fate
104 transition. In particular, we show that Wnt and SHH signaling induce cell cycle exit and molecular differentiation
105 through distinct downstream effectors, which revealed a previously unknown role for Gli3 in cell cycle exit. By
106 genetically decoupling these two graded morphogens cell cycle exit and DC differentiation occur
107 asynchronously, resulting in a gradual transition across time. Notably, we show that the observed overlapping
108 levels of Wnt and SHH during normal DC formation is caused by their ability to modulate each other, thereby
109 ensuring their paired activity and the synchronization of cell cycle arrest and DC differentiation. This study

110 provides a model to understand how other tissues may differentially combine morphogen signals to balance
111 proliferation with differentiation during patterned tissue growth.
112
113 **Results:**
114 **Cell cycle exit and molecular differentiation are tightly coupled during dermal condensate development**
115 To examine how Wnt and SHH signaling regulate the pre-DC-to-DC transition, we first characterized where
116 and when quiescence and DC gene expression occur in relationship to Wnt and SHH activity. During mouse
117 skin development, dermal condensates (DCs) emerge around E14.0-E14.5 underneath hair follicle epithelial
118 placodes (Figure 1A, S1A). DC cells express cell type markers, including *Sox2*, *Sox18*, and *Gal*. Cells
119 expressing these markers correspond to cells that are quiescent as shown by a very low rate of EdU
120 nucleotide incorporation (Figure 1B, S1B). DC marker expression also corresponds to expression of the *in vivo*
121 G1/G0 Fucci2 reporter (Figure 1C) [25,29], and virtually all *Sox2*+ cells co-express the cell cycle inhibitor,
122 p21(*Cdkn1a)* with only rare cells expressing *Cdkn1a* but not *Sox2* (Figure 1D). Thus, markers of quiescence
123 largely colocalize with cells that express DC marker genes. Using genetic lineage tracing and EdU pulse-chase
124 experiments, we previously showed that while DC cells are quiescent, they are immediate progeny of highly
125 proliferative *Dkk1*+ progenitors that are located in the upper dermis at E13.5 and later surrounding the growing
126 DC (Figure 1D, S1B) [24]. We showed that these *Dkk1*+ proliferative progenitors undergo a short phase of
127 proliferation early during morphogenesis (between approximately E13.5-E14.5) to give rise to the vast majority
128 of arrested DC cells. Thus, cell cycle exit and molecular DC differentiation occur synchronously after a phase
129 of high proliferation (Figure S1C).
130
131 We next asked where and when Wnt and SHH activity are expressed during DC formation. As SHH ligand is
132 exclusively expressed by hair follicle epithelial placodes, SHH is not active at E13.5. However at this time
133 point, Wnt signaling is activated broadly across the upper dermis (UD) in response to Wnt ligands secreted
134 from the epidermis. This Wnt activity is required for DC and hair follicle initiation [25,30]. Although Wnt activity
135 alone is not sufficient for DC gene expression, we asked if Wnt activity alone may promote quiescence
136 independent of SHH. We used *Lef1* as a canonical marker of Wnt activity, whose expression we previously
137 showed highly correlates with other known Wnt target genes (e.g., *Axin2*, *Wif1*, *Tcf7*; Figure S1C, S1D)[24,25].

138 We found that *Lef1* expression gradually decreases over the first four upper dermal cell layers with the most
139 superficial dermal layer (closest to the epidermis) showing the highest average *Lef1* expression (Figure 1E,
140 1F). Prior to SHH, we found no significant correlation between the rate of EdU incorporation and *Lef1*
141 expression levels (Figure 1E). By E14.5, SHH is secreted by placode epithelial cells, resulting in SHH
142 activation in the placode epithelium and underlying dermis (Figure 1G). Using *Ptch1* as a canonical marker of
143 SHH activity, we found that SHH activity correlates with Wnt signaling levels at E14.5, and both correlate
144 spatially with pre-DC-to-DC cell states, with highest levels of *Ptch1* and *Lef1* seen in cells that express DC
145 markers. At this point, increasing levels of both Wnt and SHH activity correlate with decreasing rates of EdU
146 incorporation and quiescence. Notably, Wnt signaling is amplified after E13.5, and the highest levels of Wnt
147 and SHH activity now correspond with cell cycle exit and DC gene expression (Figure 1H). Hence, prior to
148 SHH (E13.5), neither DC genes nor quiescence appear to be regulated by Wnt signaling levels. When
149 epithelial placodes upregulate Wnt and SHH ligands at E14.5, both dermal Wnt and SHH activity are
150 concurrently upregulated during the pre-DC-to-DC transition. During this transition, cell cycle exit and DC gene
151 expression occur synchronously.
152
153 **High Wnt activity induces cell cycle exit independent of SHH**
154 As high levels of both Wnt and SHH activity seen at E14.5 correspond to cell cycle exit and DC gene
155 expression, we asked if high levels of Wnt and/or SHH activity regulate these events. We and others showed
156 that expression of an activated form of β-catenin in the dermis induces uniformly high Wnt activity [30,31]. This
157 results in larger DCs where placodes normally form (Figure S2A), suggesting that cells with high levels of Wnt
158 signaling are primed to undergo DC differentiation upon SHH expression. To assess if increasing Wnt activity
159 to a level higher than that seen at E13.5 (when there are no detectable DC changes) can promote pre-DC
160 changes prior to SHH expression, we expressed activated β-catenin in the dermis (*Axin2CreER;βcat*$^{fl/EX3}$ or
161 Actβcat, Figure 2A) by administering tamoxifen at E11.5. To profile molecular changes induced by high Wnt
162 activation, we performed scRNA-seq analysis of dermal populations obtained from microdissected dorsolateral
163 skin from E13.5 mutant and paired control embryos. Dermal cells were analyzed after filtering cells based on
164 known dermal markers (e.g., *Col1a1*a) as previously described. As expected, the mutant dermal population
165 showed increased expression of Wnt target genes, including *Lef1*, *Axin2* and *Tcf7*, but lacked DC markers

166 (e.g., *Sox2*) or SHH target genes (Figure 2B). We next conducted differential gene expression analysis
167 between E13.5 control and Actβcat dermal cells (Supp table 1). Despite upregulation of Wnt target genes in
168 mutant dermal cells, DC markers such as *Sox2* and *Sox18* were not significantly expressed.
169 However, *Cdkn1a*, a cell cycle inhibitor expressed by DC cells at E14.5, was among the most significantly
170 upregulated genes in the Actβcat dermis, suggesting that high Wnt activation alone may induce cell cycle exit
171 independent of DC gene expression (Figure 2B). By FISH, we verified the lack of *Gli1* or *Sox2* expression in
172 the Actβcat dermis. However, significant expression of *Cdkn1a* was detected in the mutant but not in the
173 control dermis (Figure 2B, 2C). These *Cdkn1a*+ cells showed high levels of *Lef1* expression and correlated
174 with a low rate of EdU incorporation, indicating a low rate of proliferation (Figure 2C). These data demonstrate
175 that constitutive activation of Wnt signaling is sufficient to induce expression of *Cdkn1a*, independent of SHH
176 activation (Figure 2D). By E14.5, *Cdkn1a* was highly upregulated in both control and mutant DCs. However, in
177 contrast to controls in which *Cdkn1a* expression almost perfectly overlaps with *Sox2* expression, many cells
178 surrounding *Sox2*+ clusters and within the upper dermis also expressed high levels of *Cdkn1a* but not DC
179 markers in the Actβcat mutant. They also showed a low rate of EdU incorporation (Figure 2E). *Cdkn1a*+ cells
180 that co-expressed *Sox2* in the Actβcat mutant were spatially located nearest to the placode and corresponded
181 to cells with both high Wnt and high SHH activity. Notably, cells that expressed *Sox2* in the Actβcat mutant
182 showed highest *Ptch1* expression, suggesting a threshold level of SHH activity may be required for DC gene
183 expression even if high levels of Wnt activity are induced. To assess Wnt activity levels caused by expression
184 of activated β-catenin, we quantified *Lef1* levels by quantitative FISH. As expected, E13.5 Actβcat mutant
185 dermal cells showed higher levels of *Lef1* expression than control E13.5 dermal cells. By E14.5, higher levels
186 of *Lef1* are also observed in the mutant dermis compared to controls but were never greater than those seen in
187 control DC cells, indicating that dermal expression of stabilized β-catenin does not induce levels above those
188 seen physiologically in forming DCs (Figure S2B). Taken together, these results suggest that increased Wnt
189 signaling can induce quiescence independent of SHH, while DC gene expression appears to require Wnt
190 activity as well as high levels of SHH activation (Figure 2F, 2G). Hence, Wnt and SHH interact to induce cell
191 cycle exit or DC gene expression through different mechanisms during DC genesis.
192
193 **SHH cell-autonomously augments Wnt signaling to induce cell cycle exit**

194 Based on these results, we next asked how high SHH affects DC gene expression and cell cycle exit in the
195 absence of high Wnt activity. We induced uniformly high SHH activity in the dermis by expressing a
196 constitutively activated form of Smoothened (*Axin2CreER;RosaLSL-Smom2YFP* or ActSMO) at E13.5 when
197 Wnt signaling levels are low (tamoxifen E11.5; Figure 3A). Whole-mount analysis of E14.5 skin showed that
198 high SHH activation in Wnt-active upper dermal cells induced large DCs that formed autonomously without
199 placodes (Figure 3A). Interestingly, Sox2+ cells in the center of these dermal clusters lacked EdU
200 incorporation, indicating that cell cycle exit still occurred. At the same time, many Sox2+ cells in the periphery
201 were actively proliferating as shown by Sox2+/EdU+ double positive cells (Figure 3A, Figure S3A) [24]. The
202 dermal clusters in the ActSMO mutant were also diffuse and less tightly aggregated, suggesting that the
203 coordination of DC gene expression with quiescence may be critical for DC formation. This result suggests that
204 high SHH can induce both DC genes and cell cycle exit asynchronously.
205
206 We asked how quiescence can occur if high SHH was induced in cells with low Wnt activity and in the absence
207 of placodes that are typically thought to be the source of high Wnt ligands. We first measured Wnt activity in
208 the E13.5 ActSMO mutant and surprisingly found that *Lef1* levels in the ActSMO mutant were significantly
209 higher than in E13.5 controls and were similar to that seen in wildtype DC cells (Figure 3B, 3C, Figure S3A).
210 Further similar to the Actβcat mutant, these cells co-expressed high levels of *Cdkn1a* and corresponded with
211 lower rates of EdU incorporation (Figure 3D). Notably, only cells that expressed *Ptch1* (i.e., cells expressing
212 the ActSMO mutation) showed elevated *Lef1* expression while neighboring wildtype *Ptch1*-negative cells (Cre
213 non-recombined) in the upper dermis showed levels similar to the control upper dermis (Figure 3C). Thus, *Lef1*
214 expression is amplified cell-autonomously by SHH activation and possibly independent of epidermal Wnt
215 ligands. Consistent with this, we found that many cells with the highest *Lef1* transcript levels frequently were
216 not spatially closest to the epidermis where Wnt ligands are expressed (Figure 3B). Collectively, these results
217 show that SHH activation cell-autonomously accelerates Wnt activity. High Wnt activity, in turn, induces cell
218 cycle exit, These data also suggest that high levels of dermal Wnt activity seen at E14.5 may be caused by
219 SHH activation rather than by placode Wnt ligands (Figure 3E).
220

221 DC gene expression and cell cycle exit are off sync upon high SHH activation. We next sought to use this
222 model to dissect out how each process was mediated. Here, we employed an innovative computational
223 approach, GeneTrajectory (GT), to unbiasedly separate out co-occurring independent biological gene
224 programs from whole transcriptome scRNA-seq data. Briefly, GT is a computational method developed to
225 unbiasedly detect independent gene dynamics from whole transcriptome data in which each GT represents a
226 distinct biological process (Figure S3B). Traditional cell trajectory inference methods first organize cells into
227 lineages and assign a one-dimensional pseudotime and then gene dynamics are assessed with respect to
228 those cell lineages. A major limitation of these approaches arises when multiple biological processes coexist
229 within the same group of cells (e.g., when cell cycle is coupled with differentiation). Here, the inferred cell
230 pseudotime often conflates the effects of distinct processes, making it difficult to disentangle their respective
231 gene programs. By contrast, GT does not require cell trajectory inference or predefining an initial and terminal
232 cell state. It directly constructs gene trajectories and allows each cell to participate in multiple concurrent
233 biological processes. This is done by computing pairwise optimal transport distances between gene expression
234 distributions over the cell-cell graph from which gene programs, and their pseudotemporal gene order is
235 extracted based on their sequence of activation along the inferred biological processes. This separates apart
236 coexisting biological processes that are entangled at the cell level into independent gene programs with distinct
237 sequential gene expression patterns (Figure S3B).
238
239 We first used GT to examine E14.5 wildtype dermal scRNA-seq data, which identified three GTs that
240 correspond to cell cycle (CC), DC differentiation and lower dermal (LD) differentiation processes, respectively
241 (Figure 3F, Figure S3C). Here, the DC GT identifies an order of gene activity in which DC genes are expressed
242 at the terminus along with *Cdkn1a* (Figure 3F). This method was benchmarked against other cell trajectory
243 inference methods, showing superior accuracy in delineating the order of genes involved in the DC
244 differentiation process based on biological validaton[28]. We then defined different cell stages along the DC
245 differentiation process by partitioning the DC GT into gene bins, with each bin representing marker genes for a
246 specific stage. For each cell, we computed a gene bin score representing the proportion of genes from a given
247 bin that were expressed. Based on these scores, cells were exclusively assigned to a stage or left unassigned
248 (Method - Gene bin and cell stages, Figure 3F). Canonical DC genes, including *Gal*, *Sox18* and *Sox2,* were

249 largely expressed at the last stage 6 (Figure 3G). Similarly, the CC GT represents an independent process in
250 which cells are colored according to their expression of genes along a progression from S and G2/M phases
251 (Figure 3F). As shown, cells expressing genes along the DC GT also simultaneously express genes that
252 correspond to an independent cell cycle process (proliferation). Measuring the fraction of cells in G1/G0 phase
253 by DC GT stages showed that cells at stage 6 are quiescent with a G1 fraction near 1.0 (Figure 3H). At the
254 same time, both *Lef1* and *Ptch1* covary and show increasing levels across DC GT stages with highest levels of
255 both observed at stage 6 (Figure 3I). Hence as expected, Wnt activity is coupled to SHH activation in the
256 wildtype condition, and cell cycle exit and molecular DC differentiation occur simultaneously at the terminus
257 (Figure 3J).
258
259 **A gene program that corresponds to cell cycle exit is identified by GeneTrajectory**
260 Based on the observation that there were proliferating Sox2+ cells surrounding a quiescent center in the
261 ActSMO condition, this suggests that cell cycle exit does not always occur simultaneously with DC gene
262 expression. We asked if we can use GT to separate out the two processes of cell cycle exit and DC gene
263 expression in the ActSMO condition. We obtained scRNA-seq data from E13.5 ActSMO and paired control skin
264 to exclude any possible confounding effects of endogenous SHH activation and DC formation. As expected,
265 the ActSMO mutant showed uniformly high *Ptch1* expression in dermal cells, while Wnt target genes remained
266 localized to cells that express UD markers (Figure 4A). Interestingly, GT identified four GTs in the ActSMO
267 mutant: one corresponded to CC (S/G2/M) and another to LD differentiation, which were similar to the control
268 (Figure 4B, Figure S4A). As expected, one GT contained DC genes as well as Wnt target genes, which was
269 not detected in the E13.5 control. Additionally, a new GT was detected in the ActSMO mutant that was not
270 present in the E13.5 control (Figure 4B). To characterize this new gene module, we performed pathway
271 analysis. We found that genes belonging to this GT were most highly associated with regulation of TP53, which
272 is involved in tumor suppression and inhibits cell cycle progression (Figure 4C). These genes included cell
273 cycle regulators such as *Trp53inp1* and *Plk2*, which overlap with *Cdkn1a* expression (Figure 4C, Supp Table
274 1). Cells expressing this gene program were predominantly Wnt-active and restricted to G1/G0 phase (Figure
275 4B). Based on these findings, we defined this GT as a cell cycle exit GT (Exit GT). By FISH, both *Cdkn1a* and
276 *Trp53inp1* were significantly upregulated in the E13.5 ActSMO dermis compared to E13.5 control dermis,

277 which showed negligible expression of these genes (Figure 4D). We first measured Wnt activity in the E13.5
278 ActSMO mutant by measuring *Lef1* levels in *Trp53inp1*+ cells. Consistent with the ability of SHH activation to
279 cell-autonomously upregulate Lef1 levels (Figure 3C), *Trp53inp1*+ cells showed significantly higher *Lef1*
280 transcript levels than E13.5 control upper dermal cells with some *Trp53inp1*+ cells showing levels similar to
281 E14.5 wildtype DC cells (Figure 4D). In contrast to E14.5 wildtype embryos in which *Trp53inp1* and *Cdkn1a*
282 are largely restricted to *Sox2*+ DC cells, these genes were expressed by both *Sox2*+ and surrounding *Sox2*-
283 cells in the E13.5 ActSMO mutant. This indicates that Exit GT genes are expressed not exclusive in cells that
284 express terminal DC genes in the ActSMO mutant.
285
286 We next asked if this gene program can be detected in the E13.5 Actβcat mutant, which also induced cell cycle
287 exit but not DC genes. GT method also identified a similar GT in the E13.5 Actβcat dermis, which shared
288 several genes with the E13.5 ActSMO Exit GT, including *Trp53inp1* along with *Cdkn1a*, which was also
289 upregulated in cells expressing this GT (Figure S4B, S4C). To further compare these GTs across conditions,
290 we applied a module projection strategy (i.e., label transfer) to assess if a gene program is preserved in a
291 subset of cells under different conditions. We calculated the module score of the gene set in the other condition
292 and visualized local neighborhoods of cells that exhibited a high module score, indicating that the average
293 expression of the gene program is retained in that cell population. This enables the identification of shared or
294 condition-specific cell states across samples without requiring sample integration, thus avoiding potential
295 biases introduced by batch correction methods that may obscure true biological differences. Label transfer of
296 the E13.5 ActSMO Exit GT onto the E13.5 Actβcat and paired control showed that the two mutants share a
297 similar gene module and molecular cell state, which was not detected in the control sample (Figure 4E).
298 Moreover, we obtained scRNA-seq data from E13.5 Wntless cKO (*K14Cre;Wls*$^{fl/fl}$) embryos, which ablates
299 epidermal Wnt ligands, resulting in decreased dermal Wnt signaling and a lack of DCs or hair follicles (Figure
300 S4C) [30,32]. Here, an Exit gene program could not be detected upon label transfer (Figure 4E), indicating that
301 this Exit GT is Wnt-dependent. These results show that high Wnt activity alone is sufficient to induce genes
302 that regulate cell cycle exit independent of DC gene expression, and this Exit gene program is Wnt-dependent.
303 Furthermore, despite the decreased rate of proliferation seen in the Wntless cKO, an Exit GT was not

304 detected, indicating that this Exit gene program does not simply reflect prolonged G1 phase caused by slower
305 rates of proliferation.
306
307 Although some Sox2+ cells are proliferating in ActSMO dermal clusters at E14.5, most *Sox2*+ cells are
308 quiescent by E15.5, similar to wildtype E14.5 DC cells (Figure S4E). It was possible that the proliferating cells
309 in E14.5 ActSMO dermal clusters represent cells that will immediately exit the cell cycle upon cell division
310 similar to wildtype transitioning cells but continuously over days. To assess if the Exit GT represents a gene
311 program expressed by cells that are actively exiting the cell cycle, we performed EdU pulse-chase
312 experiments. First, we observed that most cells in the ActSMO mutant that express *Trp53inp1* at both E13.5
313 and E14.5 show a low rate of EdU incorporation similar to quiescent DC cells (Figure 4F). We next tested if
314 these quiescent *Trp53inp1*+ cells are recent progeny of a cell division by pulsing embryos 24 hours prior to
315 harvest. At both E13.5 and E14.5, there was a significant proportion of *Trp53inp1*+ cells that retained EdU
316 nucleotide, similar to wildtype E14.5 DC cells, indicating *Trp53inp1*+ cells are quiescent but many are progeny
317 of a recent cell division. Interestingly, we did not observe an accumulation of *Trp53inp1*+ cells over days
318 (Figure 4F), suggesting that its expression may be downregulated after a cell has undergone cell cycle exit
319 (Figure 4F). Thus, in the ActSMO condition, *Trp53inp1*+ cells represent cells that are undergoing cell cycle exit
320 continuously (Figure 4F). These data also suggest that the Exit GT reflects a process in which cells enter
321 quiescence as immediate progeny of a cell division similar to the cell cycle dynamics characteristic of the
322 normal pre-DC-to-DC transition (Figure 4G, Figure S1B).
323
324 **Loss of GLI3 chromatin binding regulates cell cycle exit downstream of high Wnt activity**
325 To next examine how elevated Wnt signaling promotes cell cycle exit, we first profiled genes differentially
326 bound by CTNNB1 in the E13.5 Actβcat mutant versus control skin. Although CTNNB1 was more bound at
327 Wnt target genes (e.g., *Sp5*, *Axin2*, *Lef1*, *Twist2*, *Tcf7*), we did not detect binding to *Cdkn1a* or any Exit GT
328 genes, nor did we detect significant binding to genes associated with cell cycle inhibition (Figure S5A, S5B).
329 These results are in keeping with other work showing that Wnt signaling is essential for upper dermal cell
330 proliferation and indirectly inhibits *Cdkn1a* expression[30]. Given the paradoxical finding that high Wnt activity
331 promotes cell cycle exit and that this high Wnt signaling is induced by SHH activation (Figure 3B, 3C) [24], we

332 asked if this cell cycle exit program is specifically induced in the context of SHH pathway mediators. We
333 reasoned that high Wnt activity and cell cycle exit normally is coupled to high SHH activity and DC gene
334 expression during DC formation. Hence, SHH effectors may cooperate with Wnt signaling to induce cell cycle
335 exit. Yet cell cycle exit is observed in the Actβcat mutant at E13.5 and independent of SHH. As *Gli1* is only
336 expressed upon SHH expression, Gli1 activator would not likely mediate this effect seen in the Actβcat
337 condition. By contrast, Wnt signaling is known to promote *Gli3* expression independent of SHH in the neural
338 tube [26]. Similarly, *Gli3* was also expressed in Wnt-active cells in both control and Actβcat dermal cells at E13.5
339 prior to SHH (Figure 5A). GLI3 acts as a SHH transcription repressor in the absence of SHH and binds to a
340 broad range of SHH target genes, including cell cycle regulators in the limb bud [33,34]. To profile genes that GLI3
341 binds and that may be regulated in the Actβcat condition, we performed CUT&RUN to identify GLI3-bound
342 genomic regions at E13.5. Surprisingly, we found reproducible global reduction of GLI3 binding to chromatin in
343 the Actβcat condition, indicated by decreased GLI3-bound read density at transcriptional start sites (Figure
344 5B). As expected, GLI motifs were the most enriched in the differentially bound regions based on HOMER de
345 novo motif analysis [35] (Figure S5C). KEGG pathway analysis also showed that those unbound regions are
346 enriched for genes involved in SHH signaling despite the fact that most canonical SHH target genes are not
347 significantly expressed (Figure 5C). This is consistent with recent work showing that GLI3 binding prior to SHH
348 is actually inert at many GLI3-bound regions and does not actually repress them[36]. We also found that loss of
349 GLI3 binding did not derepress many canonical SHH target genes, including *Ptch1* or *Gli1* (Figure S5B). By
350 western blot analysis, we confirmed that loss of GLI3 binding in the Actβcat condition was not due to
351 decreased protein expression (Figure 5D). Additionally, Gli3 remained largely expressed in its cleaved
352 repressor form in both the control and mutant, suggesting other mechanisms (e.g., other post-translational
353 modifications or cofactors) likely regulate GLI3 binding. These results show that high Wnt signaling alone
354 unexpectedly induces loss of GLI3 binding at many genomic regions independent of SHH but without
355 derepression of many of those unbound genes.
356
357 Even though many GLI3-unbound regions were not derepressed in the Actβcat mutant, we hypothesized that a
358 subset of unbound regions may be sufficient to induce cell cycle exit downstream of high Wnt activity. If so,
359 loss of Gli3 itself should be sufficient to induce cell cycle exit. We genetically ablated *Gli3* in the dermis

360 (*Axin2CreER;Gli3*$^{fl/fl}$ or Gli3 cKO; tamoxifen E11.5). At E14.5, DCs of Gli3 cKO embryos were smaller than
361 control DCs (Figure 5E, Figure S5D). Additionally, *Dkk1*+ peri-DC progenitors showed aberrant upregulation of
362 *Cdkn1a* with lower rates of EdU incorporation compared to controls in which most *Dkk1*+ cells do not express
363 *Cdkn1a* and are proliferative (Figure 5E, Figure S5D). Examination of E13.5 Gli3 cKO dermis prior to DC
364 formation also showed that *Cdkn1a* was highly upregulated similar to E13.5 Actβcat embryos and correlated
365 with a lower rate of EdU incorporation (Figure 5F). We obtained scRNA-seq data from E13.5 Gli3 cKO
366 embryos and paired controls. Examination of the Gli3 cKO dermal population showed that *Gli3* gene
367 expression was diminished, but expression of Wnt target genes was not affected, indicating that *Gli3* acts
368 downstream of high Wnt activity (Figure S5E, S5F). Also, neither canonical SHH target genes nor DC genes
369 (e.g., *Sox18*, *Gal*) were induced upon loss of *Gli3*, confirming that GLI3 binding does not repress many SHH
370 target genes (Figure S5E, S5F). Interestingly, GT identified four GTs in the Gli3 cKO dermal scRNA-seq data
371 (Figure 5G, Figure S5H). Three GTs corresponded to those found in the paired E13.5 control dermal data (UD,
372 LD, CC). An additional GT identified in the mutant data and not found in the control revealed that several of the
373 genes contained in this GT overlapped with those found in the Exit GT of the Actβcat mutant, including
374 *Trp53inp1* (Figure 5G). Similarly, most cells within this GT were confined to G1/G0 phase and aberrantly
375 expressed *Cdkn1a* (Figure 5G). We next intersected genes that were unbound by GLI3 in the E13.5 Actβcat
376 mutant to genes differentially expressed in the E13.5 Gli3 cKO versus control. Genes involved in cell cycle
377 inhibition, including *Mxd4* and *Efna5*, were upregulated and unbound in the Gli3 cKO and contained more
378 active promoter marks (H3K4me3, Figure 5H). We also found Exit GT genes, *Baiap2* and *Cpt1c*, were
379 unbound by GLI3 and upregulated.
380
381 We also transferred the Exit GT label from the ActSMO mutant to the Gli3 cKO, which identified the same Exit
382 GT population (Figure 5I), indicating that this gene program is shared among all three mutants (ActSMO,
383 Actβcat, Gli3 cKO). Similar to the ActSMO condition, *Cdkn1a*-high cells in the Gli3 cKO showed a low rate of
384 active EdU incorporation, while pulsing embryos with EdU 24 hours prior showed that a significant proportion
385 of *Cdkn1a*-high cells are progeny of a recent division (Figure 5F). These data show that both β-catenin and
386 Gli3 function in a common pathway that causes cell cycle exit. As DC genes were not expressed in the Gli3

387 cKO dermis, these data suggest that high Wnt signaling (downstream of SHH co-activation) induces loss of
388 GLI3 binding specifically to regulate cell cycle exit (Figure 5J).
389
390 **DC gene expression correlates with Wnt activity levels upon SHH activation**
391 We next examined the E13.5 ActSMO GT that corresponded to DC genes (Figure 6A, 6B). This DC GT
392 showed that the gene order correlated with known DC genes, including *Gal*, *Sox18* and *Sox2*, which
393 interestingly, were sequentially activated over DC GT stages in a manner that correlated with increasing *Lef1*
394 levels (Figure 6C, 6D). This was in contrast to the E14.5 wildtype DC GT in which DC genes were
395 simultaneously activated at the last stage when both Wnt and SHH activity are highest. As SHH target genes
396 are uniformly expressed across the dermis and no longer progresses with DC differentiation, canonical SHH
397 pathway genes were not detected in the ActSMO DC GT. These data show that high SHH activity can induce
398 DC genes in cells with varying levels of Wnt activity and not only in cells that have high levels of Wnt signaling
399 (Figure 6E). However, the level of DC genes expressed corresponds with the level of Wnt activity. This implies
400 that the synchronization of cell cycle exit with high DC gene expression seen in the wildtype scenario may
401 occur by restricting high SHH activity to cells with high Wnt signaling. As cell cycle exit occurs in cells that do
402 not express high DC genes in the ActSMO condition, the level of Wnt signaling necessary for cell cycle exit
403 would be lower than that required to express high DC genes (Figure 6E).
404
405 **Coupled Wnt and SHH gradients is sufficient to synchronize cell cycle exit with molecular**
406 **differentiation**
407 Based on the above results, cell cycle exit and expression of high DC genes are only seen in cells with coupled
408 high Wnt and high SHH activity induced by placode SHH ligand. We asked if inducing SHH ligand expression
409 across the epidermis is sufficient to accelerate Wnt activity and to couple high levels of Wnt signaling with high
410 SHH activity without placodes. Here, we genetically induced a covarying gradient of Wnt and SHH activation in
411 the upper dermis by expressing SHH ligand uniformly across the epidermis where Wnt ligands are normally
412 expressed prior to hair follicle morphogenesis (*K14Cre;Rosa-LSL-SHH* or SHH OE; Figure 7A). ScRNA-seq
413 analysis of E13.5 SHH overexpressing (SHH OE) mutant and paired control dermal cells showed that both
414 *Lef1* and *Ptch1* were expressed in an overlapping covarying pattern over the UMAP cell embedding in the

415 mutant (Figure 7B). Cells with the highest levels of *Lef1* and *Ptch1* also expressed DC genes (e.g., *Gal*, *Sox18*,
416 *Sox2*). Additionally, *Cdkn1a* was largely localized to cells expressing DC genes in contrast to ActSMO dermal
417 cells in which many *Cdkn1a*+ cells do not express many DC genes (Figure 7B, 7C). Notably, GT analysis
418 showed that only three GTs were identified that corresponded to similar gene programs identified in E14.5
419 wildtype dermal cells (i.e., CC, LD, DC; Figure 7D, Figure S7A). A separate Exit GT was not detected. Similar
420 to the E14.5 wildtype DC GT (Figure 2C), the E13.5 SHH OE DC GT showed a gene order in which Wnt and
421 SHH levels correlate with each other and with DC genes, which were restricted to the last stage (Figure 7D).
422 *Cdkn1a* was also activated together with DC genes (Figure 7D). Additionally, label transfer of the ActSMO Exit
423 GT did not detect a separate population in the SHH OE or control dermis (Figure 7E). As expected, *Lef1*
424 expression was accelerated in the SHH OE compared to the E13.5 control, with the highest levels
425 corresponding to arrest and DC genes (Figure 7F, S7B, S7D). Taken together, these data suggest that
426 covarying levels of Wnt and SHH activity synchronize cell cycle exit with DC genes and recapitulate the
427 wildtype pre-DC-to-DC transition.
428
429 Quantification of *Lef1* and *Ptch1* levels by spatial dermal layer showed that both genes covary with higher *Lef1*
430 levels in the first two layers of the dermis in the SHH OE compared to controls, consistent with SHH
431 accelerating *Lef1* levels (Figure 7F). By FISH, we found DC genes were restricted to the most superficial
432 dermal layers where both *Lef1* and *Ptch1* levels were highest and where proliferation is low (Figure 7F, Figure
433 S7B-C). We next performed GLI3 CUT&RUN in the mutant and control and found global loss of GLI3 binding
434 at genomic regions similar to the Actβcat mutant (Figure 7G, Figure S7D), indicating that loss of GLI3 binding
435 represents an endogenous molecular event during DC genesis and not simply an artifact of genetically
436 stabilizing β-catenin. As expected, we found loss of GLI3 binding at SHH target genes (*Ptch1*, *Gli1*) but now
437 with increased transcriptional activity as marked by increased H3K4Me3 signal at these genes. This suggests
438 that Gli activator may be required for expression of most SHH target genes and that GLI3 may function to
439 prime those sites for GLI activator upon SHH expression. We also detected loss of binding at cell cycle
440 regulators, *Mxd4* and *Efna5* similar to the Actβcat mutant (Figure 7H).
441

442 We next asked if we can modulate Wnt and SHH levels to recapitulate the interaction between these signals
443 and their regulated biological processes by establishing an in vitro dermal culture system. Previous attempts to
444 culture dermal papilla cells used neonatal dermal cells that contain preformed DC/dermal papilla cells[37,38].
445 However, they show limited ability to maintain DC/DP markers and immediately lose Wnt, SHH, and DC gene
446 expression. Further, these cells show poor responses to Wnt or SHH agonists. We found similar results using
447 neonatal dermal cells with only a mild increase in *Lef1* or *Ptch1* expression upon Wnt agonism with
448 CHIR99021 (CHIR) or SHH agonism (SAG), respectively (Figure S7E). Consistent with a previous report, we
449 found HDAC inhibitors incrementally augmented CHIR *Lef1* responses but had no effect on SAG responses
450 (Figure S7F). We next cultured dermal cells FACS isolated from E13.5 PDGFRαH2BGFP embryos. In contrast
451 to neonatal fibroblasts, E13.5 dermal cells showed robust dose-dependent target gene responses to either
452 CHIR or SAG after 48-72 hours of culture (Figure S7E).
453
454 Using this model, we asked if SHH activation can augment Wnt signaling by assessing the effect of SAG on
455 CHIR-induced *Lef1* gene expression. We found that SAG treatment boosted *Lef1* expression in CHIR-treated
456 cells (Figure 7I). Moreover, the fold increase in *Lef1* expression was significantly more in cells treated with
457 higher levels of CHIR (5 μM vs 2 μM) upon SAG treatment, suggesting that the amount of Wnt acceleration
458 depends on the initial levels of Wnt activity (Figure 7I). Consistent with in vivo results, high levels of CHIR
459 (5 μM) alone are sufficient to induce *Cdkn1a* expression independent of SHH activation (Figure 7J), while co-
460 treatment with CHIR and SAG induced DC genes such as *Gal* and *Sox18* (Figure 7K). Importantly, consistent
461 with our in vivo E14.5 Actβcat results (Figure S7G), DC gene induction was SAG-dependent, indicating that
462 higher levels of SHH activation is essential for DC gene expression. Altogether, these results demonstrate that
463 levels of Wnt and SHH activation can be tuned to coordinate cell cycle exit and DC gene expression and can
464 be used to recapitulate these events in vitro.
465
466 **Discussion:**

Our results fit with a scenario in which cell cycle exit is tightly coupled to differentiation. The decision to exit the cell cycle may be made in G2/M phase or in G1 phase. To explain this coupling, previous work have proposed a direct model in which cell cycle regulators can have a dual role in regulating cell cycle progression and cell type differentiation (e.g. activating cell type-specific transcription factors). Here, we reveal an unexpected mechanism in which these two processes are independently mediated but are coupled to each other due to the mere coupling of Wnt and SHH activity. In the DC system, Wnt activity levels are mechanistically dependent on SHH activation and the reason for the synchronization of cell cycle exit and molecular DC differentiation, yet the processes themselves are separable because the threshold level of Wnt activity required for cell cycle exit is less than that required for expressing maximal DC genes (Figure 6). This contrasts other models in which the processes are coupled to each other by co-dependent downstream mediators. Our results also demonstrate that two covarying gradients do not merely reflect overlapping independent signals induced by a common ligand source. Rather, the spatial gradients seen during DC formation, in part, reflect the dynamic interaction between Wnt and SHH to regulate each other and to coordinate distinct biological processes over a cell fate transition. Specifically, we show that SHH is sufficient to cell-autonomously amplify Wnt activity, and the high levels of Lef1 normally seen in DC cells may be caused by SHH co-activation rather than by local extrinsic placode Wnt ligands. In the wildtype scenario, only a subset of cells that have sufficient pre-existing Wnt activity (dermal layer 1 or peri-DC cells) will induce cell cycle exit and expression of all DC genes synchronously once their Wnt activity is accelerated by SHH co-activation (Figure 7L). Therefore, the coordination of Wnt and SHH signaling levels in pre-DC progenitors is likely due to the spatial proximity of these cells to epidermal cells that produce both SHH and Wnt ligands. However, the acceleration of Wnt signaling that initiates the pre-DC-to-DC transition is independent of epidermal Wnt ligands. How SHH boosts Wnt activity in dermal cells is unclear, but it is likely indirect, as we did not find that GLI transcription factors bind to Wnt target genes, including *Lef1*. We posit that this model may also help explain how other scenarios

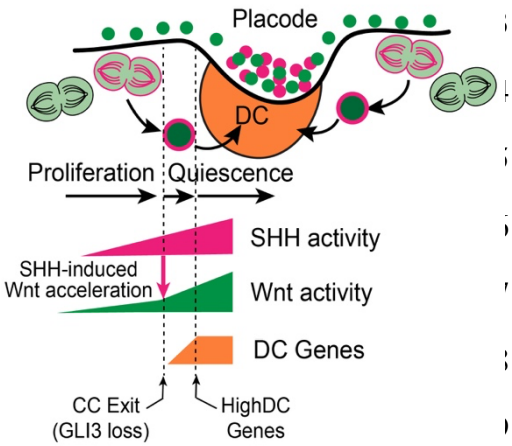

Model: Wnt and SHH ligands are secreted from epidermal cells, creating gradients of pathway activation in underlying dermal cells. SHH activation in the dermis further accelerates Wnt signaling, resulting in loss of GLI3 chromatin binding which is sufficient to cause cell cycle arrest. Concurrently, SHH activation in these high Wnt activity cells can induce DC marker genes, thereby coupling DC differentiation and cell cycle exit below the hair placode.

495 can time proliferation with differentiation. For example, hair follicle epithelial stem cells rely on Wnt and SHH
496 activation during anagen phase and give rise to transit-amplifying cells that undergo proliferation and
497 differentiation before they terminally arrest into different spatially organized cell types. It is possible that relative
498 levels of Wnt and SHH (or other signals) regulate the coordination of these two processes to time when a
499 progenitor exits the cell cycle and the specific cell type genes it expresses. From a different perspective, when
500 distinct biological processes of a cell fate transition occur synchronously, there may be few intermediate states
501 to capture the transition, giving the appearance that a population emerged from "thin air". Determining the
502 individual biological processes that induce a cell fate transition and why those processes are synchronized can
503 help address how some patterned structures appear to from without a pre-existing pattern.
504
505 In the ActSMO condition, uniformly high SHH activation was induced in cells with varying Wnt-activity, and the
506 number and expression level of DC genes correlated with Wnt signaling levels. However, in the wildtype
507 condition, DC marker genes are only expressed in cells that show both high Wnt and high SHH activity. This
508 suggests that a threshold level of SHH activity, which is induced in the ActSMO mutant, is required for DC
509 gene expression. It is plausible that high Wnt activity can reciprocally accelerate SHH activity to ensure that
510 only cells with high Wnt activity activate high SHH signaling to induce DC genes. Consistent with this, we
511 observed that cells in the peri-DC region of the E14.5 Actβcat mutant exhibited higher levels of Wnt activity
512 than control peri-DC cells but also higher *Ptch1* levels than in the control, suggesting that Wnt activity levels
513 may regulate SHH activity. Such an intricate feedback mechanism between Wnt and SHH signaling may
514 deterministically drive a rapid sequence of cell cycle exit and DC gene expression. Further studies to
515 temporally regulate Wnt and SHH activity can give insight into the intimate relationship between dermal Wnt
516 and SHH signaling.
517
518 How is cell cycle exit induced upon high Wnt activity? Wnt signaling is known to promote G1-S transition and is
519 typically associated with stemness and proliferation [7,39-41]. Consistent with this, we and others showed that loss
520 of dermal Wnt activity prior to SHH results in decreased dermal cell proliferation with concomitant loss of
521 dermal cell density [25,30]. We found that inducing high Wnt activity, above that seen prior to SHH, results in cell
522 cycle exit. This high Wnt signaling unexpectedly results in a global reduction in GLI3 binding to chromatin, and

523 loss of Gli3 is sufficient to mediate cell cycle exit. Interestingly, canonical SHH target genes such as *Ptch1* or
524 *Gli1* were not derepressed despite loss of GLI3 binding at those sites in the Actβcat mutant. These genes
525 become expressed upon SHH, suggesting GLI activator (e.g., GLI1) is required to activate those GLI sites. It
526 remains unclear how high Wnt signaling causes GLI3 unbinding. Other transcription co-factors or other GLI3
527 post-translational modifications may regulate GLI3 binding. Prior to SHH, Wnt signaling may promote GLI3
528 binding at canonical and non-canonical SHH target genes. It is possible that upon SHH, cell cycle exit is
529 immediately induced by GLI3 unbinding (after SHH-induced Wnt amplification) while DC and SHH target genes
530 may be activated soon after upon *Gli1* expression and GLI1 binding to those unbound regions. The global loss
531 of GLI3 binding upon acceleration of Wnt signaling could serve as mechanism to couple high Wnt activity with
532 efficient upregulation of SHH activity. This would ensure that DC genes are only expressed coincident with or
533 just after cell cycle exit. In the ActSMO condition, molecular DC differentiation occurs while cells are still
534 proliferating. These dermal clusters are diffuse with fuzzy borders and largely fail to contact the epidermis and
535 do not induce placodes. We hypothesize that the clustering of DC cells and their ability to communicate with
536 the epidermis relies on their ability to stop dividing and to form stable dense clusters. It will be interesting to
537 assess if cell-cell adhesion genes or extracellular matrix genes are affected by cell cycle regulators.
538
539 This study also underscores the utility of computational methods to give mechanistic insight into complex cell
540 fate transitions by separating out independent gene programs. This method was useful to identify Gli3 as a
541 molecular mediator that regulates a specific subpopulation of G1/G0 phase cells, which represent immediate
542 quiescent progeny of a division. The possibility of distinguishing heterogeneity within G1/G0 phase cells during
543 lineage specification holds the potential to uncover mechanisms that dictate if and when a cell will undergo cell
544 cycle arrest as well as how differentiation is balanced with cell divisions (e.g., asymmetric cell divisions in stem
545 cells and transit amplifying cells). From a translational perspective, this study sheds light on how distinct
546 biological processes of DC formation can be tuned to grow and differentiate DC cells *in vitro*, a critical step
547 towards making DC organoids and organotypic hair follicles to model hair growth and disease.
548
549
550 **RESOURCE AVAILABILITY**
551

552 **Lead Contact**

553 Further information and requests for resources and reagents should be directed to and will be fulfilled by the
554 lead contact, Peggy Myung (peggy.myung@yale.edu).

555 **Data and Code Availability**

556 Genomic datasets used in this study are deposited in NCBI Gene Expression Omnibus database and are
557 publicly available as of the date of publication (GSE280825, token: qfirggaarvypzet). For other all other scRNA-
558 seq data presented in this study, the data will be deposited in a GEO repository and will be made available with
559 a token upon request.

560 **EXPERIMENTAL MODEL AND SUBJECT DETAILS**

561 No statistical methods were used to predetermine sample size. The experiments were not randomized. The
562 investigators were not blinded to allocation during experiments and outcome assessment.

563 **Mice**

564 *Axin2CreER* [42] mice were bred to *Rosa-LSLSmoM2YFP* [43], *β-catenin*$^{fl(Ex3/+}$ [44] and *Gli3*$^{fl/fl}$ [45]
565 mice. *K14Cre* [46] mice were bred to *Shh* Overexpressor (Want et al. 2010) mice. *Rosa-Flag-Gli3YFP*
566 [33] mice were bred to *Axin2CreER* and *β-catenin*$^{fl(Ex3/+}$ mice to enable detection of GLI3-Flag using
567 CUT&RUN. *R26Fucci2aR* [47] reporter mice were used to visualize cell cycle phase. A random
568 population of both male and female mice were used for all experiments. All procedures involving
569 animal subjects were performed under the approval of the Institutional Animal Care and Use
570 Committee of the Yale School of Medicine.

571

572 **Acknowledgements:** We thank D. Gay, M. Ito, and R. Atit for review and discussion of this manuscript. This
573 work was supported by National Institutes of Health grants R01AR076420 (P.M.)and LEO Foundation LF-OC-
574 23-001347 (P.M.).

575

576 **Author Contributions:** Conceptualization, P.M., Y.K., R.L., Y.J., S.P.; Methodology, P.M., R.L., Y.K., Y.J.,
577 S.P.; Software, R.L., Y.K.; Resources, M.T., D.W., K.P.; Investigation, P.M., R.L., Y.J., S.P. H.L, S.V.; Writing –

578 Original Draft, P.M.; Writing – Review & Editing, P.M., R.L., Y.J., S.P., Y.K., C.L., J.L., E.B.; Supervision, P.M.,

579 Y.K.; Funding Acquisition, P.M.

580 **<u>Main Figure Titles and Legends</u>:**

581 **Figure 1: Cell cycle exit and molecular differentiation are tightly coupled during dermal condensate**
582 **development**

583 **(A)** Hair follicle development over time. (**B)** FISH images of E13.5 and E14.5 flank skin with *Sox2*+ DC with
584 lack of EdU copositivity at E14.5. (**C)** Skin whole-mount image of E14.5 Sox2eGFP skin showing GFP
585 colocalization with Fucci2 reporter. (**D)** FISH stained for indicated genes of E14.5. (**E)** FISH of E13.5 wildtype
586 skin stained for Lef1, Ptch1 or EdU after 1-hour EdU pulse, quantification of *Lef1* and *Ptch1* levels (H-score) by
587 dermal cell layer, %EdU+ by *Lef1* bin (**F)** Cartoon depicting graded *Lef1* expression spatially. (**G)** FISH of
588 E14.5 skin stained for *Lef1*, *Ptch1* or EdU; quantification of *Lef1* and *Ptch1* levels by indicated spatial regions,
589 %EdU+ by *Lef1* bin. (**H)** Cartoon depicting *Lef1* and *Ptch1* expression levels spatially; n=5. Data as mean±
590 SEM (n=5 per day); *P<0.05, **P<0.01, ***P<0.001, ****P<0.0001, one-way ANOVA; ns, not significant. Scale
591 bars, 50 µm. Related to Figure S1.

592

593 **Figure 2: High Wnt activity induces cell cycle exit independent of SHH**

594 **(A)** Cartoon of Wnt activity levels in E13.5 wildtype or Actβcat mutant (tamoxifen E11.5). (**B)** UMAP colored by
595 expression of indicated genes or cell cycle (CC) phase for E13.5 Actβcat mutant or paired control dermal
596 scRNA-seq data. (**C)** FISH showing E13.5 *Lef1*, *Cdkn1a*, EdU (left) and quantification of FISH *Cdkn1a* levels
597 (H-score) or %EdU of *Cdkn1a* (p21)+ cells. (**D)** Cartoon of cell cycle and DC molecular differentiation dynamics
598 in E13.5 Actβcat showing cells exit the cell cycle but do not express DC genes. (**E)** FISH showing E14.5 *Sox2*,
599 *Cdkn1a*, EdU (left) and FISH quantification of %EdU+ cells within indicated control or Actβcat populations. (**F)**
600 FISH showing E14.5 *Lef1*, *Ptch1*, *Sox2* (left) and FISH quantification of *Ptch1* level within indicated control or
601 Actβcat populations. (**G)** Cartoon of E14.5 Actβcat condition in which quiescence can occur without DC gene
602 expression. Related to Figure S2.

603

604 **Figure 3: SHH cell-autonomously augments Wnt signaling to induce cell cycle exit**

605 **(A)** Cartoon of experimental condition induced by expressing a constitutively activated form of Smo. Whole-
606 mount image of E14.5 ActSMO and control and quantification of %EdU+ of Sox2+ cells at E14.5. (**B**) FISH
607 showing indicated genes in control or ActSMO mutant (n=4). *Lef1* levels by **(C)** *Ptch1* status or **(D)** %EdU by

608 Lef1 levels (bin) **(E)** Cartoon showing that SHH activation cell-autonomously boosts Lef1 levels. **(F)**
609 GeneTrajectory diffusion maps and gene order and UMAPs showing DC and CC GTs. **(G)** DC gene
610 expression by DC GT stage of the E14.5 WT and UMAPs. **(H)** *Cdkn1a* expression and G1/G0 fraction by DC
611 GT stage. (I) *Lef1* and *Ptch1* levels by DC GT stage. **(J)** Cartoon of covarying Wnt and SHH activity across the
612 pre-DC-to-DC transition that corresponds to synchronous cell cycle exit and DC gene expression. Data as
613 mean± SEM; *P<0.05, **P<0.01, ***P<0.001, ****P<0.0001, one-way ANOVA. Scale bars, 50 μm. Related to
614 Figure S3.
615
616 **Figure 4: A Wnt-dependent gene program that corresponds to cell cycle exit is identified by**
617 **GeneTrajectory**
618 (**A**) UMAPs of control and ActSMO colored by indicate genes. **(B)** GT analysis of E13.5 ActSMO and paired
619 control dermal scRNA-seq data showing four GTs and DC GT of ActSMO mutant which is not present in
620 control. Exit GT of ActSMO colored by GT stage or indicated genes. **(C)** Pathway analysis of Exit GT. UMAPs
621 of control and ActSMO colored by indicate genes. **(D)** FISH showing indicated genes of E13.5 control or
622 ActSMO mutant skin; corresponding quantification of *Trp53inp1* or *Cdkn1a* levels. **(E)** Label transfer of E13.5
623 ActSMO Exit GT onto indicated E13.5 mutants. **(F)** EdU pulse-chase experiments of E13.5-E14.5 ActSMO
624 mutant and corresponding quantification of %EdU positive of *Trp53inp1*+ cells. (**G**) Cartoons depict the
625 interpretation of cell cycle dynamics of *Trp53inp1*+ cells which represent cells that are immediate progeny of a
626 division. Data as mean ± SEM, one-way ANOVA. Scale bars, 50 μm. Related to Figure S4.
627
628 **Figure 5: Loss of GLI3 chromatin binding regulates cell cycle exit downstream of high Wnt activity**
629 **(A)** FISH image of E13.5 wildtype skin showing Gli3 expression prior to SHH. **(B)** Heat map of GLI3 binding at
630 all transcriptional start sites (TSS) in E13.5 control or Actβcat mutant skin. **(C)** KEGG pathway analysis of GLI3
631 unbound regions in the Actβcat mutant. (D**)** Western blot of cell lysates from control of Actβcat mutant stained
632 for anti-Flag (Gli3) or b-actin. (**E)** FISH of E14.5 control and Gli3 cKO for indicated genes or EdU; quantification
633 of #Sox2+ cells per DC and Cdkn1a transcript levels by skin population. **(F)** FISH images of E13.5 control and
634 Gli3 cKO with indicated genes or EdU; Quantification of Cdkn1a transcripts or %EdU by population after 1-hour
635 EdU pulse or after 24-hour pulse-chase. **(G)** GT analysis of E13.5 Gli3 cKO showing an Exit GT. **(H)** Volcano

636 plot of differentially expressed genes in the Gli3 cKO vs control and those genes that overlap with GLI3
637 unbound genes in the Actβcat mutant (blue); genome browser tracks showing binding signal of respective
638 antibodies at the promoter region of indicated genes. **(I)** Label transfer of E14.5 Actβcat Exit GT onto indicated
639 mutant scRNA-seq data. **(J)** Cartoon showing model of mechanism by which high Wnt activity induces cell
640 cycle exit. Data as mean± SEM; *P<0.05, **P<0.01, ***P<0.001, ****P<0.0001, one-way ANOVA; ns, not
641 significant; scale bars, 50 μm. Related to Figure S5.
642
643 **Figure 6: DC gene expression correlates with Wnt activity levels upon SHH activation**
644 **(A)**GT analysis of E13.5 ActSMO and paired control dermal scRNA-seq data showing four GTs and DC GT
645 of ActSMO mutant which is not present in control. **(B)** DC gene expression by DC GT stage of the ActSMO
646 mutant and UMAPs. **(C)** Expression level of indicated DC genes by DC GT stage and UMAPS with indicated
647 genes. **(D)** Lef1 levels by DC GT stage. **(E)** Cartoon showing that SHH activation cell-autonomously boosts
648 Lef1 levels. Data as mean± SEM; *P<0.05, **P<0.01, ***P<0.001, ****P<0.0001, one-way ANOVA. Scale bars,
649 50 μm. Related to Figure S6.
650
651 **Figure 7: Coupled Wnt and SHH gradients is sufficient to synchronize cell cycle exit with molecular**
652 **differentiation**
653 **(A)** Cartoon of wildtype scenario showing covarying gradients and experimental scenario to induce covarying
654 Wnt and SHH gradients by expressing SHH ligand coordinately with Wnt ligands in the epidermis. (**B**) UMAPs
655 colored by gene or cell cycle phase of control and E13.5 SHH OE mutant dermal cells. (**C**) Quantification of the
656 fraction of *Cdkn1a*+ cells that co-express DC genes (Gal) in ActSMO vs SHH OE. **(D)** GT analysis of E13.5
657 SHH OE dermal scRNA-seq data. **(E)** Label transfer of E13.5 ActSMO Exit GT onto SHH OE and control
658 dermal populations. **(F)** Lef1 levels by DC GT stage; FISH image showing spatially covarying gradients of
659 Ptch1 and Lef1 that corresponds to dermal layer. **(G)** Heat map of GLI3 binding at all TSS in E13.5 control
660 versus SHH OE showing global loss of binding. **(H)** Genome browser tracks showing binding signal of
661 respective antibodies at the promoter region of indicated genes. **(I)** qPCR for *Lef1* of E13.5 PDGFRaH2B
662 dermal cells after SAG and/or CHIR stimulation for 48 hours (n=4). **(J)** qPCR for *Cdkn1a* after 48 hours. (K)
663 qPCR for DC genes after 48 hours of culture with CHIR and/or SAG. **(L)** Model of how gradient levels of Wnt

664 and SHH interact dynamically to coordinate DC differentiation gene expression and cell cycle exit and that the
665 covariance of the two signals is responsible for the synchronization of cell cycle exit and DC genes during DC
666 genesis. Data as mean ± SEM, one-way ANOVA; scale bars, 50 μm. Related to Figure S7.
667
668

669 **STAR Methods**

670 **Key resources table**

REAGENT or RESOURCE	SOURCE	IDENTIFIER
Antibodies		
Rabbit anti-IgG	EpiCypher	Cat#13-0042; RRID: AB_2923178
Rabbit anti-H3K4Me3	EpiCypher	Cat#13-0041; RRID: AB_3076423
Rabbit anti-H3K27Ac	EpiCypher	Cat#13-0059; RRID: AB_2923489
Chicken anti-GFP	Abcam	Cat#Ab13970; RRID: AB_300798
Rabbit anti-Sox2	Abcam	Cat#Ab97959; RRID: AB_2341193
Mouse anti-Flag	Millipore	Cat#F1804; RRID: AB_262044
Rabbit anti-RFP	Rockland	Cat# 600-401-379; RRID: AB_2209751
Rabbit anti-CTNNB1	Antibodies-online	Cat#ABIN2855042; RRID: AB_10825282
Donkey anti-rabbit Alexa Fluor 488	Thermo Fisher Scientific	Cat#A21206; RRID: AB_2535792
Goat anti-chicken Alexa Fluor 488	Thermo Fisher Scientific	Cat#A11039; RRID: AB_2534096
Donkey anti-rabbit Alexa Fluor 568	Thermo Fisher Scientific	Cat#A10042; RRID: AB_2534017
Chemicals, peptides, and recombinant proteins		
Hoechst	Invitrogen	H3570
DAPI solution	Novus Biologicals	Cat#NBP2-31156
Tamoxifen	Sigma Aldrich	Cat#T5648
EdU (5-ethynyl-2-deoxyuridine)	Thermo Fisher Scientific	Cat#E10187
CHIR99021	Sigma-Aldrich	Cat#SML-1046
SAG	Sigma-Aldrich	Cat#SML-1314
Critical commercial assays		
Click it EdU Imaging Kit 555	Invitrogen	Cat#C10338
Click it EdU Imaging Kit 488	Invitrogen	Cat#A10266
RNAscope Multiplex Fluorescent Detection Kit v2	ACDBio	Cat#323270
Deposited data		
Raw sequence data files	NCBI Gene Expression Omnibus	GEO: GSE280825
Experimental models: Organisms/strains		
Mouse: β−catenin EX3/+	Harada et al., 1999	N/A
Mouse: Axin2CreER	Amerongen et al., 2012	N/A
Mouse: Fucci2	Abe et al., 2013	N/A
Mouse: K14Cre	Dassule et al., 2000	N/A
Mouse: Wls flox/flox	Carpenter et al., 2010	N/A
Mouse: Sox2eGFP	Arnold et al., 2011	N/A
Mouse: R26R-LSL-SmoM2YFP	Jeong et al., 2004	N/A
Mouse: Gli3 flox/flox	Blaess S et al., 2008	N/A
Mouse: *Gli3*^{3XFlag}	Lopez-Rios J , et al., 2014	N/A
Mouse: *lox-EGFP-STOP-lox-Shh*	PI: David Wang, University of Michigan Ann Arbor	N/A
Mouse: PDGFRaH2BGFP	Hamilton et al., 2003	N/A
Oligonucleotides		
Mouse-Cdkn1a	ACDBio	Cat#408551
Mouse-Ptch1	ACDBio	Cat#402811
Mouse-Lef1	ACDBio	Cat#441861
Mouse-Sox2	ACDBio	Cat#401041
Mouse-Trp53inp1	ACDBio	Cat#1161531

Mouse-Gli3	ACDBio	Cat#445511
Mouse-Dkk1	ACDBio	Cat#402521
Mouse-Gal	ACDBio	Cat#400961
Software and algorithms		
Adobe photoshop CC 2024	Adobe Systems	http://www.adobe.com/products/photoshop.html
Adobe Illustrator CC 2024	Adobe Systems	http://www.adobe.com/products/illustrator/features.html
Fiji	National Institutes of Health	https://imagej.net/software/fiji/
R	R Core Team	https://www.r-project.org/
rARPACK	R Package	https://cran.r-project.org/web/packages/rARPACK/index.html
Differential Abundance analysis	Landa et al., 2020	https://arxiv.org/abs/2011.03418
Seurat	Macosko et al., 2015	http://satijalab.org/seurat/
GraphPad Prism 9.1.0	GraphPad software	https://www.graphpad.com/scientific-software/prism/

METHOD DETAILS

Tamoxifen induction of mice

Embryos were staged as days post coitum, with embryonic day E0.5 considered as noon of the day a vaginal plug was detected after overnight mating. Pregnant dams were given one dose of Tamoxifen dissolved in corn oil (20mg/ml, Sigma) at 40-60 µg/gm body weight by oral gavage at E11.5 as indicated.

EdU Incorporation Assay

To assess active proliferation, EdU was administered to pregnant mice intraperitoneally (25 µg/gm) and embryos were harvested after 1.5 hour. For pulse-chase experiments, 25 µg/gm EdU was administered to pregnant mice at indicated times and embryos were harvested at later times. EdU incorporation was assessed using the Click-it EdU Imaging kit Alexa 555 or Alexa 488 (Life technologies, c10338) according to manufacturer's instructions. Briefly, skin explants were treated with a mixture of 1X Click-iT reaction buffer, $CuSO_4$, Alexa Fluor azide dye and 1X reaction buffer additive, all provided in the Click-it EdU Imaging Kit, for 30 minutes at RT before washing in PBS.

Histology

10% formalin-fixed paraffin embedded (FFPE) whole embryos were used for histological analysis. FFPE embryos were sectioned at 10 µm thickness for FISH.

Whole mount immunofluorescence

Dorsolateral skin from embryos were microdissected and placed on nucleopore filters (VWR, WHA 800281) and fixed overnight with 4%PFA at 4° C. Skin explants were blocked for 6 hours in 5% normal donkey serum,

691 1% bovine serum albumin and 0.5% Triton-X100 at RT. Explants were incubated overnight at 4° C in the
692 following primary antibodies: rabbit anti-Sox2 (1:400, Abcam, ab97959), chicken anti-GFP (1:500, Abcam,
693 ab13970), rabbit anti-RFP (1:500, Rockland, 600-401-379). Explants were then washed in 0.2% Tween20/PBS
694 for 4-6 hours on a rotator and then incubated with the following secondary antibodies: Alexa Fluor 568-donkey
695 anti-rabbit (1:200, Invitrogen, A10042), Alexa Fluor 488-donkey anti-rabbit (1:200, Invitrogen, A21206), Alexa
696 Fluor 488-goat anti-chicken (1:200, Invitrogen, A11039) overnight at RT. Washes were carried out for 6 hours
697 with 0.2% Tween20/PBS. Hoechst (1:750 in PBS) was used for 45 min before mounting on slides with
698 SlowFade Gold Antifade Mountant (Invitrogen, S36936).

699 *In-situ* hybridization

700 The RNAscope Multiplex Fluorescent Detection Kit v2 (ACDBio, 323110) was used for single-molecule
701 fluorescence in situ hybridization (FISH) according to the manufacturer's protocol. Briefly, sections were
702 deparaffinized and permeabilized with hydrogen peroxide followed by antigen retrieval and protease treatment
703 before probe hybridization. After hybridization, amplification and probe detection were done using the Amp 1–3
704 reagents. Probe channels were targeted using the provided HRP-C1-3 reagents and tyramide signal
705 amplification VIVID fluorophores—650 and 570 (ACD biotechne, 323271). EdU staining was done using the
706 Click-it EdU Imaging Kit Alexa 488 (Life Technologies, c10338) according to the manufacturer's instructions.
707 Nuclear counter-stain was done using Hoechst 33342 (Invitrogen, H3570) before mounting with SlowFade
708 Mountant. RNA scope probes used (ACDBio)—Mm-Lef1 (441861), Mm-Ptch1 (402811), Mm-Dkk1 (402521),
709 Mm-Sox2 (401041), Mm-Gal (400961), Mm-Gli3 (400961) and Mm-Trp53inp1 (1161531).

710 Microscopy

711 FISH paraffin-embedded images were acquired using the Leica Stellaris 8 DMi8 confocal microscope with a
712 ×40 oil immersion (Numerical Aperture 1.3) objective lens, scanned at 5 μm thickness, 1, 024 × 1, 024 pixel
713 width, 400Hz. Whole mount explants were imaged in 3 dimensions using the LaVision TriM Scope II (LaVision
714 Biotec) microscope equipped with a Chameleon Vision II (Coherent) two-photon laser (810 -1000 nm) to
715 acquire *z*-stack images ranging from 50-120 μm (2 μm serial optical sections) using a 20X water immersion
716 lens (NA 1.0; Olympus), scanned with a field of view of 0.3–0.5 mm^2 at 800 Hz.

717 Single-cell dissociation

718 Embryonic dorsolateral/flank skin was micro-dissected and pooled after genotyping (3 embryos per condition)
719 and dissociated into a single-cell suspension using 0.25% trypsin (Gibco, Life Technologies) for 14 minutes at
720 37° C. Single-cell suspensions were then stained with DAPI (Fisher Scientific, NBP2-31156) just prior to
721 fluorescence-activated cell sorting.

722 Fluorescence-activated cell sorting

723 DAPI-excluded live skin cells were sorted on a BD FACS Aria II (Biosciences) sorter with a 100 μm nozzle.
724 Cells were sorted in bulk and submitted for 10X Genomics library preparation at 0.75-1.0x10^6/mL concentration
725 in 4% FCS/PBS solution.

726 Single-cell RNA sequencing and library preparation

727 Chromium Single cell 3' Library and Gel Bead Kit v2 Chromium Single Cell 3′ Library & Gel Bead Kit v2 (PN-
728 120237), Chromium Single Cell 3′ Chip kit v2 (PN-120236) and Chromium i7 Multiplex Kit (PN-120262) were
729 used according to the manufacturer's instructions in the Chromium Single Cell 3′ Reagents Kits V2 User
730 Guide. After cDNA libraries were created, they were subjected to Novaseq 6000 (Illumina) sequencing.

731 10X scRNA-seq data pipeline to matrix

732 The transcriptomes of live single cells from E13.5 or E14.5 mouse skin samples under different biological
733 conditions were sequenced. Raw 10X sequencing data was processed into a matrix employing the standard
734 10X CellRanger pipeline. Briefly, base call files were fastq format which were aligned to the mm10 reference
735 genome followed by nUMI and barcode counting, constructing the nUMI count matrices. nUMI matrices were
736 filtered, centered and normalized using Seurat@1. Briefly, for each original run condition (e.g., E13.5 wildtype),
737 cells with > 1,000 detected genes, mitochondrial content < 25%, and ribosomal content > 5% (calculated via
738 PercentageFeatureSet in Seurat) were retained. Doublets were identified and removed using scDblFinder@2.
739 Data were then log-normalized by total UMI count.

740 Principal Component Calculation and UMAP Visualization

741 Principal components were computed using Seurat's RunPCA on the top 2,000 variable genes. The number of
742 PCs retained was determined from the elbow plot@7, and used for downstream analysis, including
743 dimensionality reduction for visualization and clustering.

744 Cell type specification

745 For each original run, UMAP was performed on log-normalized, centered, and scaled UMI count matrices
746 using the retained PCs. Unsupervised clustering was then conducted using Seurat's FindClusters function with
747 a resolution of 0.5. Clusters expressing Col1a1 were defined as dermal, while clusters expressing Lef1 or Dkk1
748 were defined as upper-dermal.

749 Gene trajectory inference

750 We applied GeneTrajectory@3 to each sample to identify multiple, independent gene dynamic processes. For
751 each sample, we followed the recommended guidelines. We selected the top 2,000 highly variable genes
752 (identified using Seurat's FindVariableFeatures) that were expressed in >1% and <50% of cells as input. The
753 top 20PCs were used to compute a diffusion map, and the top 10 diffusion components were used to construct
754 a cell k-nearest neighbor graph (k = 10).

755 The number of gene trajectories and the time steps for gene inclusion within each trajectory were determined
756 interactively by inspecting the top three or more gene embeddings. For the samples analyzed in this study, we
757 identified the following gene trajectories and associated time steps (t):

758 • E14.5 wild type: 3 trajectories (t = 13, 10, 5)
759 • E13.5 SmoM2: 4 trajectories (t = 1, 3, 2, 1); control: 3 trajectories (t = 3, 2, 2)
760 • E13.5 TG: 3 trajectories (t = 6, 3, 3); control: 3 trajectories (t = 5, 3, 3)
761 • E13.5 EX3: 4 trajectories (t = 3, 3, 2, 2); control: 3 trajectories (t = 1, 3, 3)
762 • E13.5 Gli3-KO: 4 trajectories (t = 8, 7, 6, 1); control: 3 trajectories (t = 4, 3, 1)

763 Gene bins and cell stages

764 Following GeneTrajectory guidelines, each trajectory from mutant samples was divided into 5 or 6 gene bins.
765 For each bin, a gene bin score was computed for both mutant and control samples to compare gene
766 expression dynamics across the cell embedding. Cell involved in each trajectory were stratified into the same
767 number of stages, based on whether they expressed more than 50% of the genes in the corresponding gene
768 bin. Cells assigned to multiple stages were resolved by assigning them to the stage closer to the terminal end
769 of the trajectory (i.e., farther from the branching point).

770 Exit GT Score

771 Exit GT scores for each sample were calculated using Seurat's AddModuleScore, based on all genes from the
772 exit gene trajectory identified in E13.5 SmoM2.

773 Pathway enrichment analysis

774 Reactome pathway enrichment analysis was performed using ReactomePA@4, with pathways showing $p <$
775 0.05 considered significantly enriched.

776 Cell cycle estimation of scRNA-seq data

777 We employed Seurat's cell cycle scoring [48]. Briefly, averaged relative expression of those cell cycle related
778 genes were used to calculate G2/M and S scores, which were used for binning cells into G2/M, S and G1/G0
779 bins.

780 Data merge and normalization

781 For comparative analysis, we merged upper-dermal cell matrices from each pair of conditions separately (i.e.
782 E13.5 control and Gli3-KO), followed by standard preprocessing and normalization using the workflow provided
783 by Seurat.

784 Differential abundance and Differential gene expression analysis

785 Differential abundant cells were identified using DA-seq@6, with a DA score threshold > 0.8. Differential gene
786 expression analysis between DA cells from E13.5 Gli3-KO and all other upper-dermal cells from both E13.5
787 Gli3-KO and control was performed using Seurat's FindMarkers without prefiltering. Significant DEGs for
788 visualization were defined using a combined threshold of padj < 1e-5 and log2FC > 0.23.

789 CUT&RUN experiments

790 CUT&RUN was performed with the Epicypher CUTANA™ ChIC/CUT&RUN Kit (14-1048) according to the
791 manufacturer's specifications with the following conditions: 500,000 cells per sample were prepared first and
792 nuclei were extracted according to the Epicypher CUT&RUN Manual Appendix. Nuclei were incubated with
793 activated ConA beads. The following antibodies (0.5 ug of antibody per reaction) were used:
794 IgG Control antibody: CUTANA™ Kit Rabbit IgG CUT&RUN Negative Control Antibody, EpiCypher Rabbit anti-
795 H3K27Ac antibody, Millipore Mouse anti-Flag antibody, Antibodies-online Rabbit anti-CTNNB1 antibody.
796 Libraries were prepared using the Epicypher CUTANA™ CUT&RUN Library Prep Kit (14-1002) according to
797 the manufacturer's specifications. Library quality was analyzed using Agilent Tapestation D1000 High
798 Sensitivity Tapes (#5067-5584). Sequencing was performed with 5 million 150bp paired-end reads per sample
799 on an Illumina NovaSeq 6000.

800 CUT&RUN data analysis

801 CUT&RUN reads were analyzed for quality using FastQC
802 (https://www.bioinformatics.babraham.ac.uk/projects/fastqc/) and adaptors trimmed using Trimmomatic. Reads
803 were then aligned to mm9 by Bowtie2 version 2.3.1. SAMTools version 1.11 was then used to convert to BAM
804 format, index, isolate uniquely mapped paired reads, and remove duplicates. MACS2 version 2.2.8 was used
805 to call peaks with IgG as input control. Read counts across genomic intervals and peak visualization were
806 performed using deepTools version 3.5 and bigwig files were visualized using the Integrative Genomics
807 Viewer. Deseq2 was used to identify differentially bound peaks between conditions, DiffBind used to plot
808 heatmaps of accessible/bound regions and HOMER to identify *de novo* motifs most enriched in the
809 differentially bound regions and annotate associated genes.

810 Western blot

811 Cells were lysed in RIPA buffer (Thermo Fisher Scientific, Cat# 89900) supplemented with protease inhibitors
812 (Thermo Fisher Scientific, Cat# 87786) for 30 minutes at 4 °C. The lysates were clarified by centrifugation at
813 10,000 × g for 20 minutes at 4 °C, and protein concentrations were determined using Bradford Protein Assay
814 Kit (Bio-Rad, Cat# 5000006). Equal amounts of protein (10 µg) were denatured at 95 °C for 5 minutes and
815 loaded onto 4–12% precast polyacrylamide gels (Bio-Rad, Cat# 3450125) for electrophoresis. Proteins were
816 transferred to PVDF membranes (Thermo Fisher Scientific, Cat# IB24001) using an iBlot2 transfer device
817 (Invitrogen, Cat# IB21001). Membranes were blocked with 5% BSA (vol/vol) in 1× TBST (AmericanBio, Cat#
818 AB14330-01000) at room temperature, incubated with primary antibodies overnight at 4 °C, washed three
819 times with TBST for 5 minutes each, incubated with HRP-conjugated secondary antibodies for 1 hour at room
820 temperature, and washed again three times with TBST.
821 Membranes were developed using SuperSignal West Pico PLUS Chemiluminescent Substrate (Thermo Fisher
822 Scientific, Cat# 34577) and imaged on a ChemiDoc imaging system (Bio-Rad). The following antibodies were
823 used: mouse anti-Flag (Millipore, Cat# F1804), rabbit anti-Actin (Cell Signaling Technology, Cat# 4970), HRP-
824 conjugated goat anti-rabbit IgG (Cell Signaling Technology, Cat# 7074), and HRP-conjugated goat anti-mouse
825 IgG (Bio-Rad, Cat# STAR207P, 1:10,000).

826 Dermal cell culture

827 E13.5 PDGFRαH2BGFP skin cells were sorted based on their GFP status. GFP+ cells were collected and
828 pelleted (300 × g, 10 min, 4°C), resuspended at 2×10^6 cells/mL in complete growth medium (DMEM + 10%

829 FBS, Penicillin-Streptomycin, and L-Glutamine), and viability was assessed by trypan blue exclusion. Cells
830 were plated at 3×10^6 cells/well in 6-well plates in 2 mL total volume. For chemical perturbation assays, cells
831 were mixed 1:1 with a 2× agonist solution. For example, 10 μM CHIR99021 (Sigma, Cat# SML1046) was
832 prepared in DMSO and diluted to a working concentration of 5 μM in culture. Similarly, SAG (Sigma, Cat#
833 SML1314) was prepared as a 50 μM stock and diluted as needed. Media with agonist was used fresh or stored
834 at 4°C for up to two days. Cells were cultured in 48-72 hours.

835 qPCR

836 Total RNA was extracted from cultured cells using the RNeasy Mini Kit (Qiagen, Cat# 74134) according to the
837 manufacturer's protocol. Complementary DNA (cDNA) was synthesized from 500 ng–1 μg of total RNA using
838 the SuperScript™ III First-Strand Synthesis System (Invitrogen, Cat# 18080051) with random hexamer
839 primers. Quantitative PCR was performed using the PowerUp™ SYBR™ Green Master Mix (Thermo Fisher
840 Scientific, Cat# 4364344) on a Viia7 Real-Time PCR System (Applied Biosystems) in 384-well optical plates.
841 Reactions were run in technical triplicates using gene-specific primers, and threshold cycle (Ct) values were
842 normalized to Gapdh as a housekeeping gene. Relative expression was calculated using the ΔΔCt method.
843

844 **QUANTIFICATION AND STATISTICAL ANALYSIS**

845 Image analysis

846 Raw image stacks acquired from whole-mount explants were imported into Fiji or Adobe Photoshop for
847 analysis. ggplot2 and cowplot R libraries were used for graphical representation of the scRNA-seq data.
848 Diffusion maps were generated as described above.

849 Quantification

850 For quantification of DC density, 3-dimensional whole-mount tiled mosaics of skin explants with a 1000 x 1000
851 μm field of view and a z-depth of 60-100 μm were used for n=3-4 embryos. For volumetric quantification of DC
852 cell number, EdU+ or Tom+ percentage of DC or UD, 3-dimensional whole mount mosaics stained with Sox2
853 and EdU or RFP were used to manually count positive cells, using ImageJ (Fiji) software using planar (XY) and
854 orthogonal (YZ, XZ) views. For volumetric quantification of cell cycle phases, 3-dimensional whole mount
855 mosaics stained with markers for G0/G1 cells (based on Fucci2 reporter) were done manually by counting
856 nuclear positive cells using ImageJ (Fiji) software. For quantification of upper dermal cells, a distance of 10 um

857 below the epidermis was considered upper dermis. For quantification of the peri-DC region by whole-mount,
858 cells two cell layers out from the Sox2+ DC were counted. For quantification based on FISH, cells with 4-5 dots
859 were considered positive (according to the RNAScope manufacturer's instructions) and sections from a total of
860 n=4 different embryos were examined. To measure RNA expression levels, H-scores were calculated
861 according to ACDBio manufacturer's instructions: a cell with 0 dot is scored 0, 1-3 dots score 1, 4-9 dots score
862 2, 10-15 dots and/or less than 10% clustered dots score 3, and more than 15 dots and/or more than 10%
863 clustered dots score 4; then the final H-score of a given cell type A is calculated by summing the (% cells
864 scored B within all cells in A)*B for score B in 0-4. For quantification of upper dermal cells, a distance of 10-20
865 μm below the epidermis was considered as upper dermis. For quantification of cells in the peri-DC region
866 *Dkk1*+*Sox2*- was considered.

867 Statistical analysis

868 All statistical values are expressed as mean ± SEM. An unpaired Student's *t*-test was used to analyze data
869 sets with two groups and $^{*}P < 0.05$ to, $^{**}P < 0.01$, $^{***}P < 0.001$ and $^{****}P < 0.00001$ indicated a significant
870 difference. When comparing more than two groups, *P* values were determined by one-way ANOVA with
871 Tukey's HSD test performed as the post hoc analysis. Statistical calculations were performed using Prism
872 software package (GraphPad). For categorical data, a chi-square test was employed to estimate a *P* value.
873
874

875 References

876 1. Soufi, A., and Dalton, S. (2016). Cycling through developmental decisions: how cell cycle dynamics
877 control pluripotency, differentiation and reprogramming. Development *143*, 4301-4311.
878 10.1242/dev.142075.
879 2. Liu, L., Michowski, W., Kolodziejczyk, A., and Sicinski, P. (2019). The cell cycle in stem cell
880 proliferation, pluripotency and differentiation. Nat Cell Biol *21*, 1060-1067. 10.1038/s41556-019-0384-
881 4.
882 3. Pauklin, S., and Vallier, L. (2013). The cell-cycle state of stem cells determines cell fate propensity. Cell
883 *155*, 135-147. 10.1016/j.cell.2013.08.031.

884 4. Calder, A., Roth-Albin, I., Bhatia, S., Pilquil, C., Lee, J.H., Bhatia, M., Levadoux-Martin, M., McNicol,
885 J., Russell, J., Collins, T., and Draper, J.S. (2013). Lengthened G1 phase indicates differentiation status
886 in human embryonic stem cells. Stem Cells Dev *22*, 279-295. 10.1089/scd.2012.0168.
887 5. Nguyen, L., Besson, A., Roberts, J.M., and Guillemot, F. (2006). Coupling cell cycle exit, neuronal
888 differentiation and migration in cortical neurogenesis. Cell Cycle *5*, 2314-2318. 10.4161/cc.5.20.3381.
889 6. Theilgaard-Monch, K., Pundhir, S., Reckzeh, K., Su, J., Tapia, M., Furtwangler, B., Jendholm, J.,
890 Jakobsen, J.S., Hasemann, M.S., Knudsen, K.J., et al. (2022). Transcription factor-driven coordination
891 of cell cycle exit and lineage-specification in vivo during granulocytic differentiation : In memoriam
892 Professor Niels Borregaard. Nat Commun *13*, 3595. 10.1038/s41467-022-31332-1.
893 7. Greco, V., Chen, T., Rendl, M., Schober, M., Pasolli, H.A., Stokes, N., Dela Cruz-Racelis, J., and Fuchs,
894 E. (2009). A two-step mechanism for stem cell activation during hair regeneration. Cell Stem Cell *4*,
895 155-169. 10.1016/j.stem.2008.12.009.
896 8. Hsu, Y.C., Li, L., and Fuchs, E. (2014). Transit-amplifying cells orchestrate stem cell activity and tissue
897 regeneration. Cell *157*, 935-949. 10.1016/j.cell.2014.02.057.
898 9. Yi, R. (2017). Concise Review: Mechanisms of Quiescent Hair Follicle Stem Cell Regulation. Stem
899 Cells *35*, 2323-2330. 10.1002/stem.2696.
900 10. Sun, Q., Lee, W., Hu, H., Ogawa, T., De Leon, S., Katehis, I., Lim, C.H., Takeo, M., Cammer, M.,
901 Taketo, M.M., et al. (2023). Dedifferentiation maintains melanocyte stem cells in a dynamic niche.
902 Nature *616*, 774-782. 10.1038/s41586-023-05960-6.
903 11. Cotsarelis, G., Sun, T.T., and Lavker, R.M. (1990). Label-retaining cells reside in the bulge area of
904 pilosebaceous unit: implications for follicular stem cells, hair cycle, and skin carcinogenesis. Cell *61*,
905 1329-1337.
906 12. Morita, R., Sanzen, N., Sasaki, H., Hayashi, T., Umeda, M., Yoshimura, M., Yamamoto, T., Shibata, T.,
907 Abe, T., Kiyonari, H., et al. (2021). Tracing the origin of hair follicle stem cells. Nature *594*, 547-552.
908 10.1038/s41586-021-03638-5.

909 13. Ouspenskaia, T., Matos, I., Mertz, A.F., Fiore, V.F., and Fuchs, E. (2016). WNT-SHH Antagonism
910 Specifies and Expands Stem Cells prior to Niche Formation. Cell *164*, 156-169.
911 10.1016/j.cell.2015.11.058.
912 14. Rompolas, P., Deschene, E.R., Zito, G., Gonzalez, D.G., Saotome, I., Haberman, A.M., and Greco, V.
913 (2012). Live imaging of stem cell and progeny behaviour in physiological hair-follicle regeneration.
914 Nature *487*, 496-499. 10.1038/nature11218.
915 15. Zhang, C., Wang, D., Wang, J., Wang, L., Qiu, W., Kume, T., Dowell, R., and Yi, R. (2021). Escape of
916 hair follicle stem cells causes stem cell exhaustion during aging. Nat Aging *1*, 889-903. 10.1038/s43587-
917 021-00103-w.
918 16. Driskell, R.R., Lichtenberger, B.M., Hoste, E., Kretzschmar, K., Simons, B.D., Charalambous, M.,
919 Ferron, S.R., Herault, Y., Pavlovic, G., Ferguson-Smith, A.C., and Watt, F.M. (2013). Distinct fibroblast
920 lineages determine dermal architecture in skin development and repair. Nature *504*, 277-281.
921 10.1038/nature12783.
922 17. Myung, P., Andl, T., and Atit, R. (2022). The origins of skin diversity: lessons from dermal fibroblasts.
923 Development *149*. 10.1242/dev.200298.
924 18. Chuong, C.M., Widelitz, R.B., Ting-Berreth, S., and Jiang, T.X. (1996). Early events during avian skin
925 appendage regeneration: dependence on epithelial-mesenchymal interaction and order of molecular
926 reappearance. J Invest Dermatol *107*, 639-646.
927 19. Hardy, M.H. (1992). The secret life of the hair follicle. Trends Genet *8*, 55-61.
928 20. Millar, S.E. (2002). Molecular mechanisms regulating hair follicle development. J Invest Dermatol *118*,
929 216-225. 10.1046/j.0022-202x.2001.01670.x.
930 21. Paus, R., Muller-Rover, S., Van Der Veen, C., Maurer, M., Eichmuller, S., Ling, G., Hofmann, U.,
931 Foitzik, K., Mecklenburg, L., and Handjiski, B. (1999). A comprehensive guide for the recognition and
932 classification of distinct stages of hair follicle morphogenesis. J Invest Dermatol *113*, 523-532.
933 10.1046/j.1523-1747.1999.00740.x.

934 22. Saxena, N., Mok, K.W., and Rendl, M. (2019). An updated classification of hair follicle morphogenesis.
935 Exp Dermatol *28*, 332-344. 10.1111/exd.13913.
936 23. Chase, H.B., Rauch, R., and Smith, V.W. (1951). Critical stages of hair development and pigmentation
937 in the mouse. Physiol Zool *24*, 1-8. 10.1086/physzool.24.1.30152098.
938 24. Qu, R., Gupta, K., Dong, D., Jiang, Y., Landa, B., Saez, C., Strickland, G., Levinsohn, J., Weng, P.L.,
939 Taketo, M.M., et al. (2022). Decomposing a deterministic path to mesenchymal niche formation by two
940 intersecting morphogen gradients. Dev Cell *57*, 1053-1067 e1055. 10.1016/j.devcel.2022.03.011.
941 25. Gupta, K., Levinsohn, J., Linderman, G., Chen, D., Sun, T.Y., Dong, D., Taketo, M.M., Bosenberg, M.,
942 Kluger, Y., Choate, K., and Myung, P. (2019). Single-Cell Analysis Reveals a Hair Follicle Dermal
943 Niche Molecular Differentiation Trajectory that Begins Prior to Morphogenesis. Dev Cell *48*, 17-31 e16.
944 10.1016/j.devcel.2018.11.032.
945 26. Alvarez-Medina, R., Cayuso, J., Okubo, T., Takada, S., and Marti, E. (2008). Wnt canonical pathway
946 restricts graded Shh/Gli patterning activity through the regulation of Gli3 expression. Development *135*,
947 237-247. 10.1242/dev.012054.
948 27. Xu, Z., Wang, W., Jiang, K., Yu, Z., Huang, H., Wang, F., Zhou, B., and Chen, T. (2015). Embryonic
949 attenuated Wnt/beta-catenin signaling defines niche location and long-term stem cell fate in hair follicle.
950 Elife *4*, e10567. 10.7554/eLife.10567.
951 28. Qu, R., Cheng, X., Sefik, E., Stanley Iii, J.S., Landa, B., Strino, F., Platt, S., Garritano, J., Odell, I.D.,
952 Coifman, R., et al. (2024). Gene trajectory inference for single-cell data by optimal transport metrics.
953 Nat Biotechnol. 10.1038/s41587-024-02186-3.
954 29. Biggs, L.C., Makela, O.J., Myllymaki, S.M., Das Roy, R., Narhi, K., Pispa, J., Mustonen, T., and
955 Mikkola, M.L. (2018). Hair follicle dermal condensation forms via Fgf20 primed cell cycle exit, cell
956 motility, and aggregation. Elife *7*. 10.7554/eLife.36468.
957 30. Chen, D., Jarrell, A., Guo, C., Lang, R., and Atit, R. (2012). Dermal beta-catenin activity in response to
958 epidermal Wnt ligands is required for fibroblast proliferation and hair follicle initiation. Development
959 *139*, 1522-1533. 10.1242/dev.076463.

960 31. Zhang, Y., Andl, T., Yang, S.H., Teta, M., Liu, F., Seykora, J.T., Tobias, J.W., Piccolo, S., Schmidt-
961 Ullrich, R., Nagy, A., et al. (2008). Activation of beta-catenin signaling programs embryonic epidermis
962 to hair follicle fate. Development *135*, 2161-2172. 10.1242/dev.017459.
963 32. Fu, J., and Hsu, W. (2013). Epidermal Wnt controls hair follicle induction by orchestrating dynamic
964 signaling crosstalk between the epidermis and dermis. J Invest Dermatol *133*, 890-898.
965 10.1038/jid.2012.407.
966 33. Vokes, S.A., Ji, H., Wong, W.H., and McMahon, A.P. (2008). A genome-scale analysis of the cis-
967 regulatory circuitry underlying sonic hedgehog-mediated patterning of the mammalian limb. Genes Dev
968 *22*, 2651-2663. 10.1101/gad.1693008.
969 34. te Welscher, P., Zuniga, A., Kuijper, S., Drenth, T., Goedemans, H.J., Meijlink, F., and Zeller, R.
970 (2002). Progression of vertebrate limb development through SHH-mediated counteraction of GLI3.
971 Science *298*, 827-830. 10.1126/science.1075620.
972 35. Heinz, S., Benner, C., Spann, N., Bertolino, E., Lin, Y.C., Laslo, P., Cheng, J.X., Murre, C., Singh, H.,
973 and Glass, C.K. (2010). Simple combinations of lineage-determining transcription factors prime cis-
974 regulatory elements required for macrophage and B cell identities. Mol Cell *38*, 576-589.
975 10.1016/j.molcel.2010.05.004.
976 36. Lex, R.K., Zhou, W., Ji, Z., Falkenstein, K.N., Schuler, K.E., Windsor, K.E., Kim, J.D., Ji, H., and
977 Vokes, S.A. (2022). GLI transcriptional repression is inert prior to Hedgehog pathway activation. Nat
978 Commun *13*, 808. 10.1038/s41467-022-28485-4.
979 37. Park, M., Jang, S., Chung, J.H., Kwon, O., and Jo, S.J. (2021). Inhibition of class I HDACs preserves
980 hair follicle inductivity in postnatal dermal cells. Sci Rep *11*, 24056. 10.1038/s41598-021-03508-0.
981 38. Kishimoto, J., Burgeson, R.E., and Morgan, B.A. (2000). Wnt signaling maintains the hair-inducing
982 activity of the dermal papilla. Genes Dev *14*, 1181-1185.
983 39. Choi, Y.S., Zhang, Y., Xu, M., Yang, Y., Ito, M., Peng, T., Cui, Z., Nagy, A., Hadjantonakis, A.K.,
984 Lang, R.A., et al. (2013). Distinct functions for Wnt/beta-catenin in hair follicle stem cell proliferation

985 and survival and interfollicular epidermal homeostasis. Cell Stem Cell *13*, 720-733.
986 10.1016/j.stem.2013.10.003.
987 40. Huggins, I.J., Bos, T., Gaylord, O., Jessen, C., Lonquich, B., Puranen, A., Richter, J., Rossdam, C.,
988 Brafman, D., Gaasterland, T., and Willert, K. (2017). The WNT target SP5 negatively regulates WNT
989 transcriptional programs in human pluripotent stem cells. Nat Commun *8*, 1034. 10.1038/s41467-017-
990 01203-1.
991 41. Myung, P.S., Takeo, M., Ito, M., and Atit, R.P. (2013). Epithelial Wnt ligand secretion is required for
992 adult hair follicle growth and regeneration. J Invest Dermatol *133*, 31-41. 10.1038/jid.2012.230.
993 42. van Amerongen, R., Bowman, A.N., and Nusse, R. (2012). Developmental stage and time dictate the
994 fate of Wnt/beta-catenin-responsive stem cells in the mammary gland. Cell Stem Cell *11*, 387-400.
995 10.1016/j.stem.2012.05.023.
996 43. Jeong, J., Mao, J., Tenzen, T., Kottmann, A.H., and McMahon, A.P. (2004). Hedgehog signaling in the
997 neural crest cells regulates the patterning and growth of facial primordia. Genes Dev *18*, 937-951.
998 10.1101/gad.1190304.
999 44. Harada, N., Tamai, Y., Ishikawa, T., Sauer, B., Takaku, K., Oshima, M., and Taketo, M.M. (1999).
000 Intestinal polyposis in mice with a dominant stable mutation of the beta-catenin gene. EMBO J *18*,
001 5931-5942. 10.1093/emboj/18.21.5931.
002 45. Blaess, S., Stephen, D., and Joyner, A.L. (2008). Gli3 coordinates three-dimensional patterning and
003 growth of the tectum and cerebellum by integrating Shh and Fgf8 signaling. Development *135*, 2093-
004 2103. 10.1242/dev.015990.
005 46. Dassule, H.R., Lewis, P., Bei, M., Maas, R., and McMahon, A.P. (2000). Sonic hedgehog regulates
006 growth and morphogenesis of the tooth. Development *127*, 4775-4785.
007 47. Abe, T., Sakaue-Sawano, A., Kiyonari, H., Shioi, G., Inoue, K., Horiuchi, T., Nakao, K., Miyawaki, A.,
008 Aizawa, S., and Fujimori, T. (2013). Visualization of cell cycle in mouse embryos with Fucci2 reporter
009 directed by Rosa26 promoter. Development *140*, 237-246. 10.1242/dev.084111.

010 48. Nestorowa, S., Hamey, F.K., Pijuan Sala, B., Diamanti, E., Shepherd, M., Laurenti, E., Wilson, N.K.,
011 Kent, D.G., and Gottgens, B. (2016). A single-cell resolution map of mouse hematopoietic stem and
012 progenitor cell differentiation. Blood *128*, e20-31. 10.1182/blood-2016-05-716480.
013

Figure 1

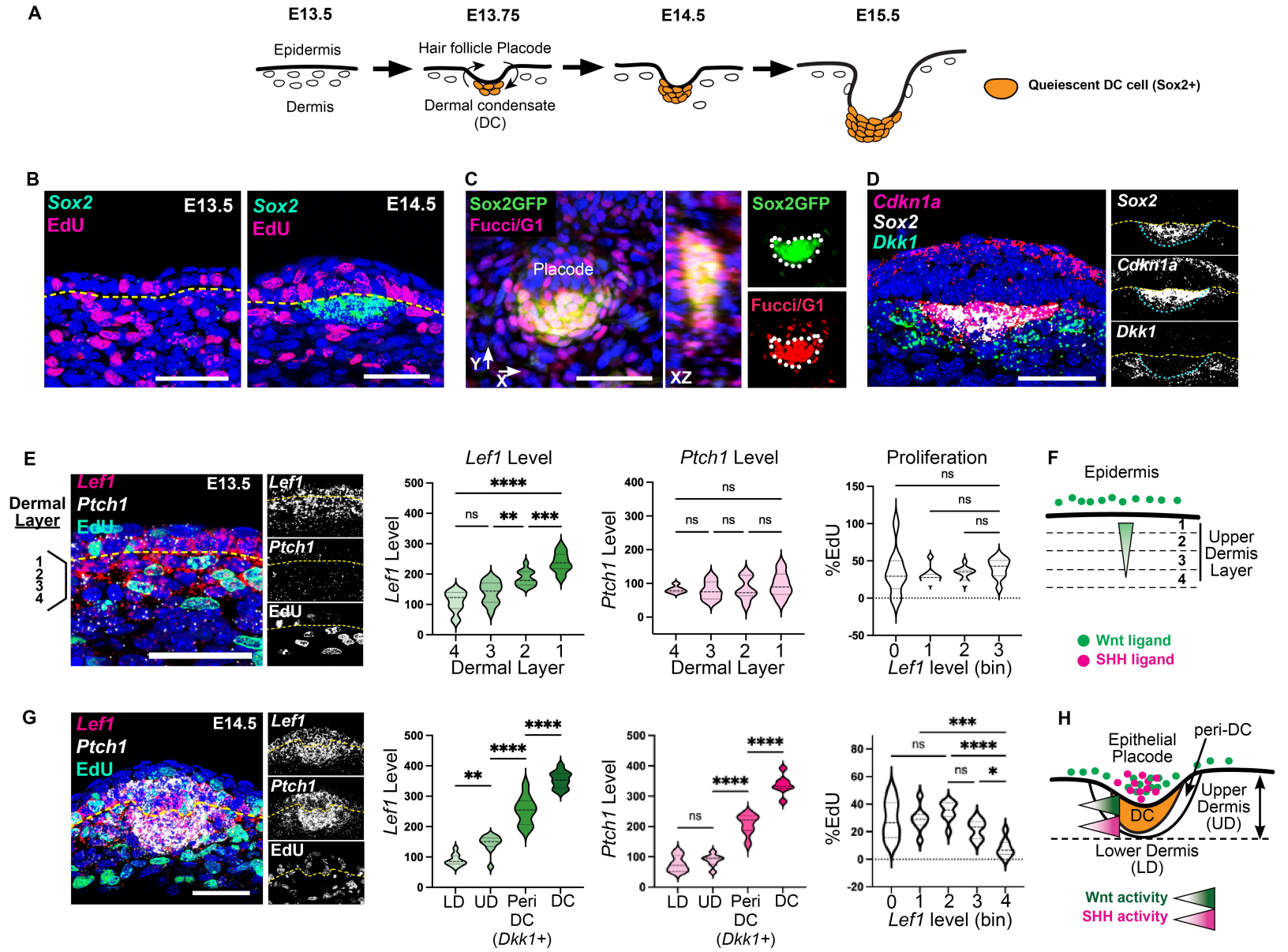
A
E13.5
E13.75
E14.5
E15.5
Epidermis
Dermis
Hair follicle Placode
Dermal condensate (DC)
Queiescent DC cell (Sox2+)
B
Sox2
EdU
E13.5
E14.5
C
Sox2GFP
Fucci/G1
Placode
XZ
D
Cdkn1a
Sox2
Dkk1
E
Dermal Layer
Lef1
Ptch1
EdU
Lef1 Level
Ptch1 Level
Proliferation
Dermal Layer
%EdU
Lef1 level (bin)
F
Epidermis
Upper Dermis Layer
Wnt ligand
SHH ligand
G
LD
UD
Peri DC
DC (Dkk1+)
H
Epithelial Placode
peri-DC
DC
Upper Dermis (UD)
Lower Dermis (LD)
Wnt activity
SHH activity

Figure 2

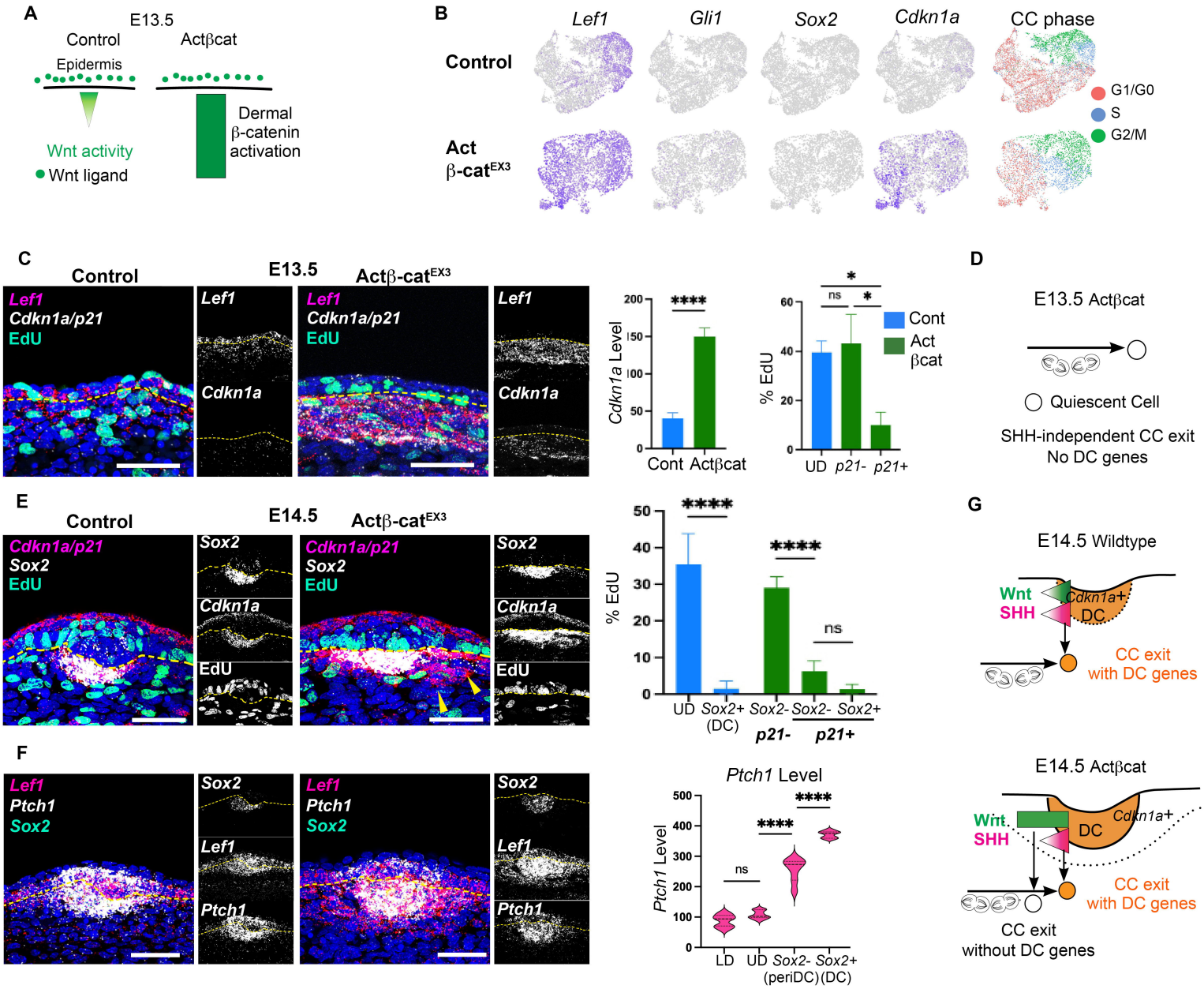

A
E13.5
Control
Actβcat
Epidermis
Wnt activity
Wnt ligand
Dermal β-catenin activation
B
Lef1
Gli1
Sox2
Cdkn1a
CC phase
Control
Act β-cat^EX3
G1/G0
S
G2/M
C
Control
E13.5
Actβ-cat^EX3
Lef1
Cdkn1a/p21
EdU
Cdkn1a
Cdkn1a Level
Cont
Actβcat
% EdU
UD
p21-
p21+
ns
D
E13.5 Actβcat
Quiescent Cell
SHH-independent CC exit
No DC genes
E
Control
E14.5
Actβ-cat^EX3
Cdkn1a/p21
Sox2
EdU
% EdU
UD
Sox2+ (DC)
Sox2-
p21-
p21+
G
E14.5 Wildtype
Wnt
SHH
Cdkn1a+
DC
CC exit with DC genes
F
Lef1
Ptch1
Sox2
Ptch1 Level
LD
UD
Sox2- (periDC)
Sox2+ (DC)
E14.5 Actβcat
CC exit without DC genes

Figure 3

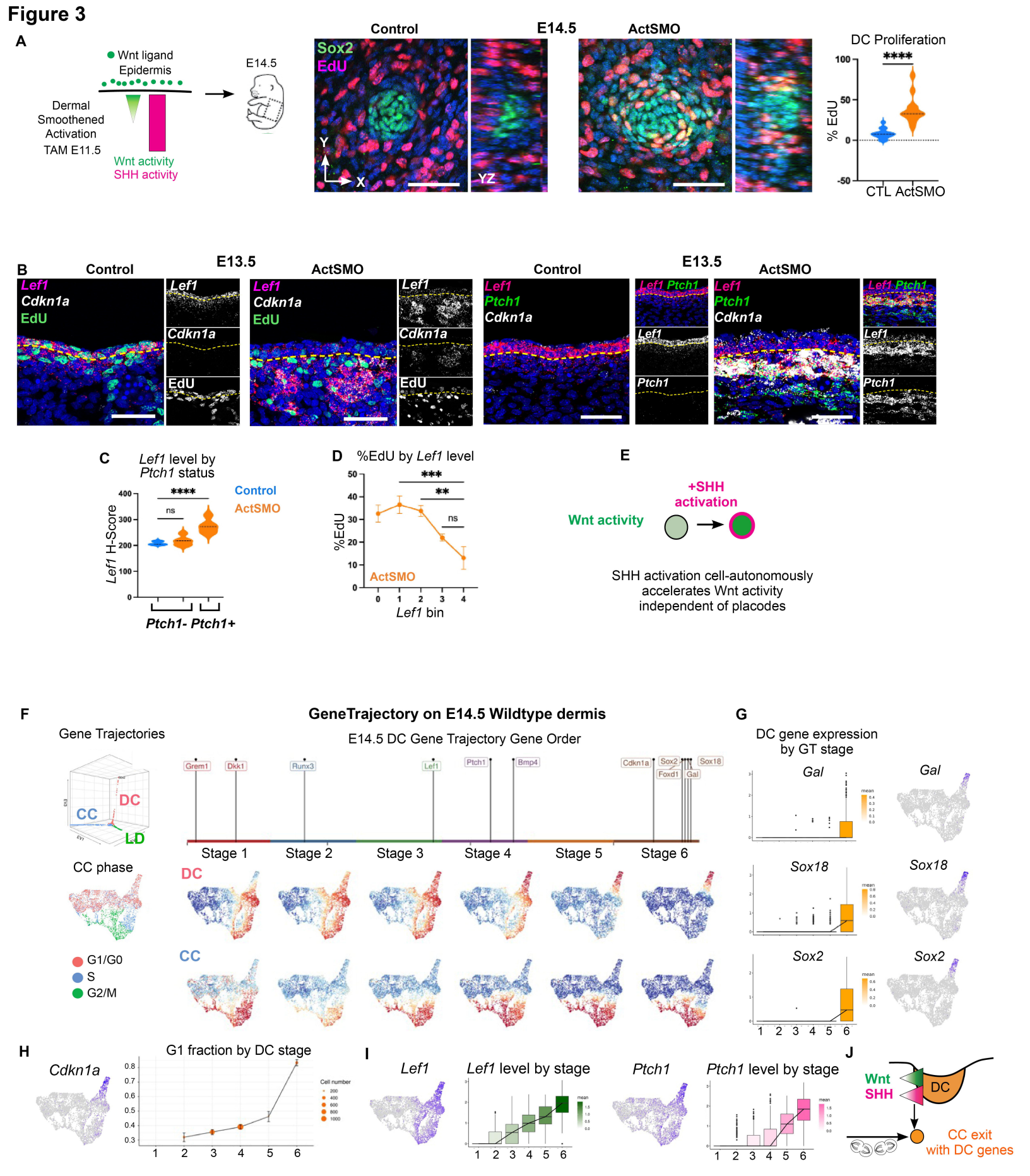
A
Wnt ligand
Epidermis
Dermal
Smoothened
Activation
TAM E11.5
Wnt activity
SHH activity
E14.5
Control
E14.5
ActSMO
Sox2
EdU
Y
X
YZ
DC Proliferation
****
% EdU
100
50
0
-50
CTL ActSMO
B
Control
E13.5
ActSMO
Lef1
Cdkn1a
EdU
Ptch1
Lef1 Ptch1
C
Lef1 level by
Ptch1 status
Lef1 H-Score
****
ns
Control
ActSMO
Ptch1- Ptch1+
D
%EdU by Lef1 level
%EdU
***
**
ns
ActSMO
Lef1 bin
E
+SHH
activation
Wnt activity
SHH activation cell-autonomously
accelerates Wnt activity
independent of placodes
F
GeneTrajectory on E14.5 Wildtype dermis
Gene Trajectories
E14.5 DC Gene Trajectory Gene Order
Grem1
Dkk1
Runx3
Lef1
Ptch1
Bmp4
Cdkn1a
Sox2
Foxd1
Gal
Sox18
DC
CC
LD
Stage 1
Stage 2
Stage 3
Stage 4
Stage 5
Stage 6
CC phase
G1/G0
S
G2/M
G
DC gene expression
by GT stage
Gal
Sox18
Sox2
H
Cdkn1a
G1 fraction by DC stage
Cell number
I
Lef1
Lef1 level by stage
Ptch1
Ptch1 level by stage
J
Wnt
SHH
DC
CC exit
with DC genes

Figure 4

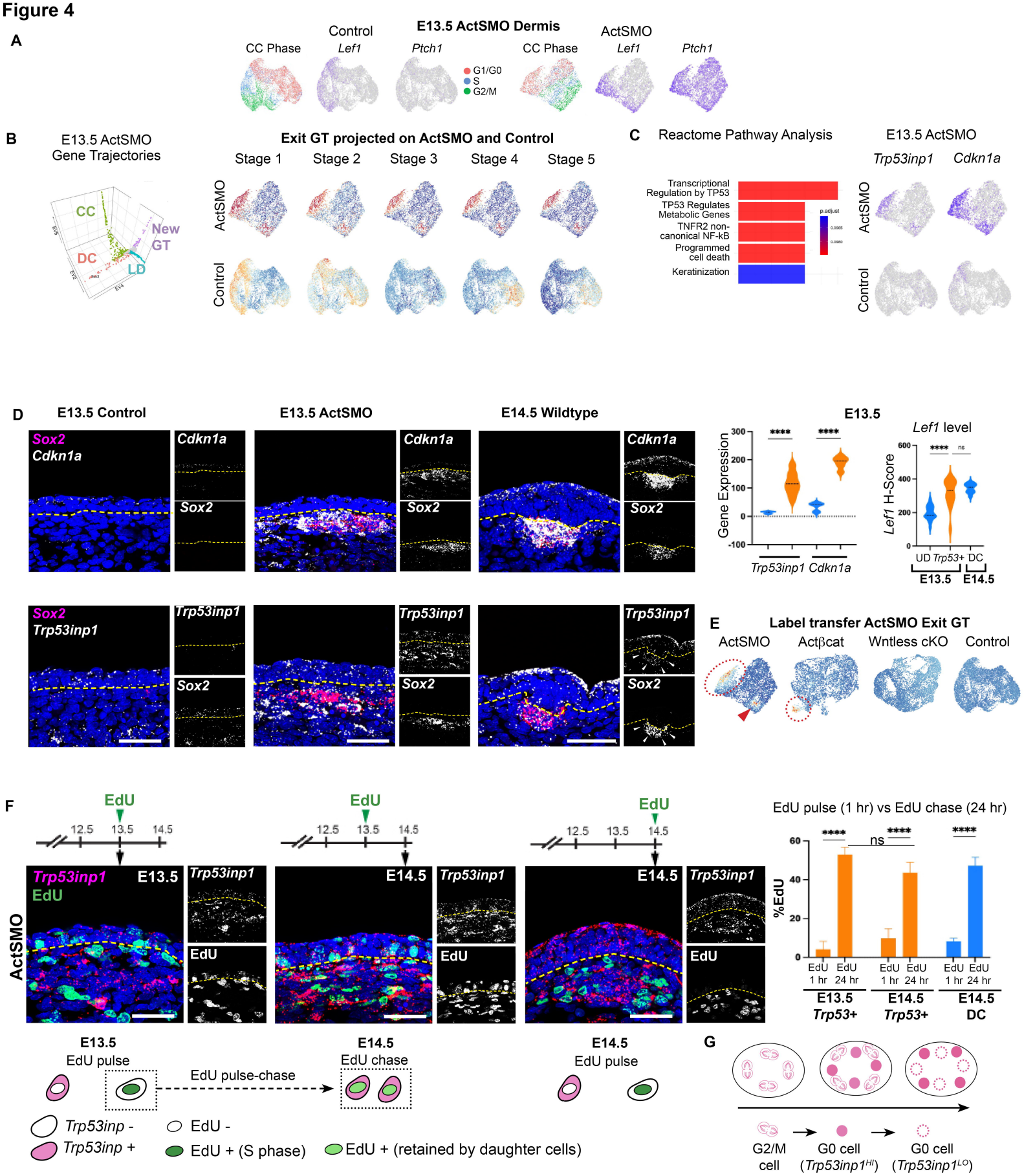
A
E13.5 ActSMO Dermis
Control
ActSMO
CC Phase
Lef1
Ptch1
CC Phase
Lef1
Ptch1
G1/G0
S
G2/M
B
E13.5 ActSMO
Gene Trajectories
CC
DC
LD
New GT
Exit GT projected on ActSMO and Control
Stage 1
Stage 2
Stage 3
Stage 4
Stage 5
ActSMO
Control
C
Reactome Pathway Analysis
Transcriptional Regulation by TP53
TP53 Regulates Metabolic Genes
TNFR2 non-canonical NF-kB
Programmed cell death
Keratinization
p.adjust
E13.5 ActSMO
Trp53inp1
Cdkn1a
ActSMO
Control
D
E13.5 Control
E13.5 ActSMO
E14.5 Wildtype
Sox2
Cdkn1a
Trp53inp1
E13.5
Gene Expression
Trp53inp1
Cdkn1a
Lef1 level
Lef1 H-Score
UD
Trp53+
DC
E13.5
E14.5
E
Label transfer ActSMO Exit GT
ActSMO
Actβcat
Wntless cKO
Control
F
EdU
12.5
13.5
14.5
Trp53inp1
EdU
E13.5
E14.5
ActSMO
EdU pulse (1 hr) vs EdU chase (24 hr)
%EdU
ns
EdU 1 hr
EdU 24 hr
E13.5 Trp53+
E14.5 Trp53+
E14.5 DC
E13.5
EdU pulse
EdU pulse-chase
E14.5
EdU chase
E14.5
EdU pulse
Trp53inp -
Trp53inp +
EdU -
EdU + (S phase)
EdU + (retained by daughter cells)
G
G2/M cell
G0 cell (Trp53inp1HI)
G0 cell (Trp53inp1LO)

Figure 5

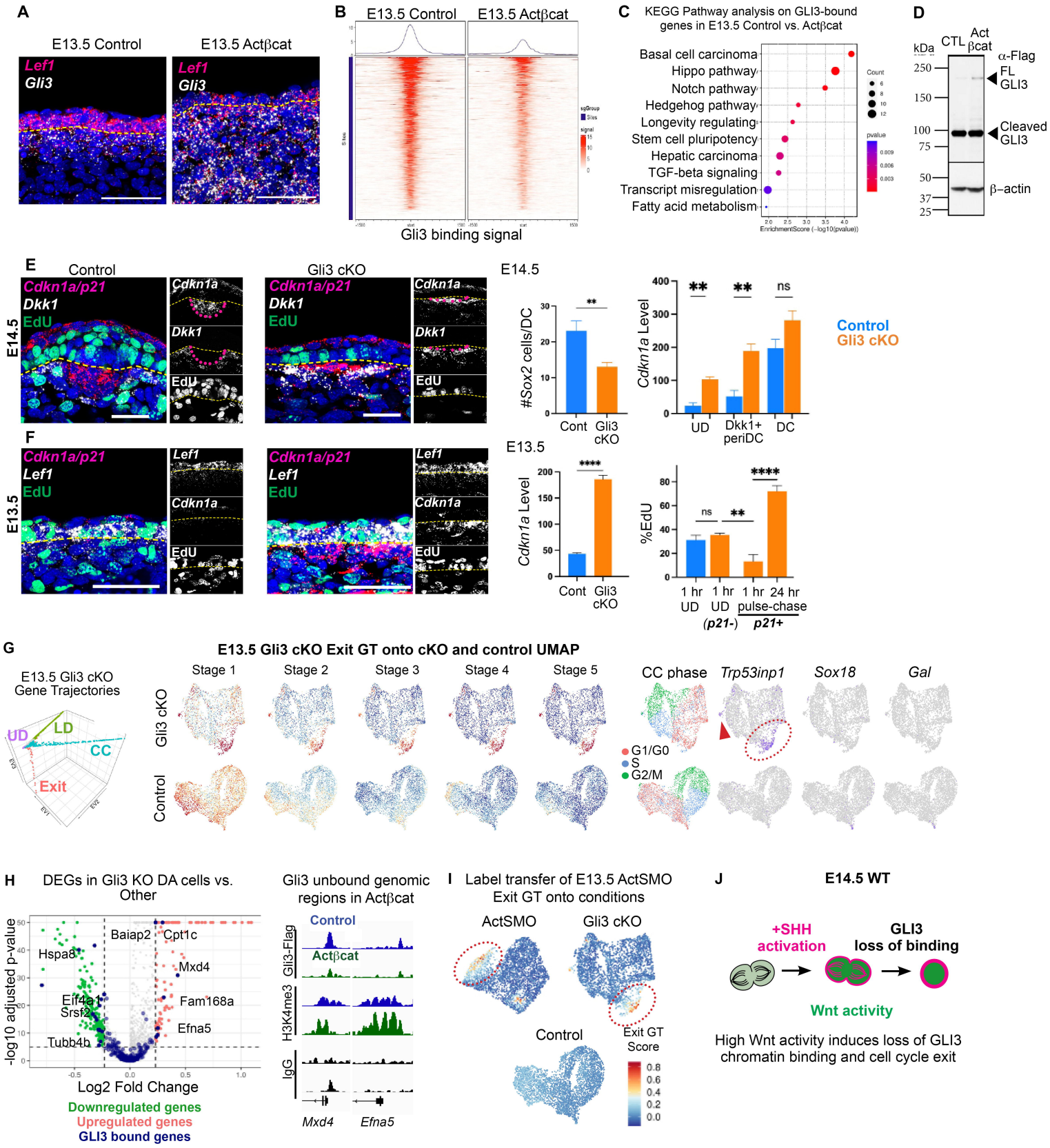
A
E13.5 Control
E13.5 Actβcat
Lef1
Gli3
B
E13.5 Control
E13.5 Actβcat
Gli3 binding signal
C
KEGG Pathway analysis on GLI3-bound genes in E13.5 Control vs. Actβcat
Basal cell carcinoma
Hippo pathway
Notch pathway
Hedgehog pathway
Longevity regulating
Stem cell pluripotency
Hepatic carcinoma
TGF-beta signaling
Transcript misregulation
Fatty acid metabolism
EnrichmentScore (−log10(pvalue))
Count
pvalue
D
kDa
CTL
Act βcat
α-Flag
FL GLI3
Cleaved GLI3
β-actin
250
150
100
75
50
37
25
E
Control
Gli3 cKO
E14.5
Cdkn1a/p21
Dkk1
EdU
Cdkn1a
#Sox2 cells/DC
Cdkn1a Level
Cont
Gli3 cKO
UD
Dkk1+ periDC
DC
ns
Control
Gli3 cKO
F
E13.5
Cdkn1a/p21
Lef1
EdU
Cdkn1a
%EdU
1 hr UD
1 hr UD
1 hr
24 hr
pulse-chase
(p21-)
p21+
G
E13.5 Gli3 cKO Exit GT onto cKO and control UMAP
E13.5 Gli3 cKO Gene Trajectories
UD
LD
CC
Exit
Stage 1
Stage 2
Stage 3
Stage 4
Stage 5
CC phase
Trp53inp1
Sox18
Gal
Gli3 cKO
Control
G1/G0
S
G2/M
H
DEGs in Gli3 KO DA cells vs. Other
Baiap2
Cpt1c
Hspa8
Mxd4
Eif4e1
Srsf2
Fam168a
Efna5
Tubb4b
-log10 adjusted p-value
Log2 Fold Change
Downregulated genes
Upregulated genes
GLI3 bound genes
Gli3 unbound genomic regions in Actβcat
Control
Actβcat
Gli3-Flag
H3K4me3
IgG
Mxd4
Efna5
I
Label transfer of E13.5 ActSMO Exit GT onto conditions
ActSMO
Gli3 cKO
Control
Exit GT Score
J
E14.5 WT
+SHH activation
GLI3 loss of binding
Wnt activity
High Wnt activity induces loss of GLI3 chromatin binding and cell cycle exit

Figure 6

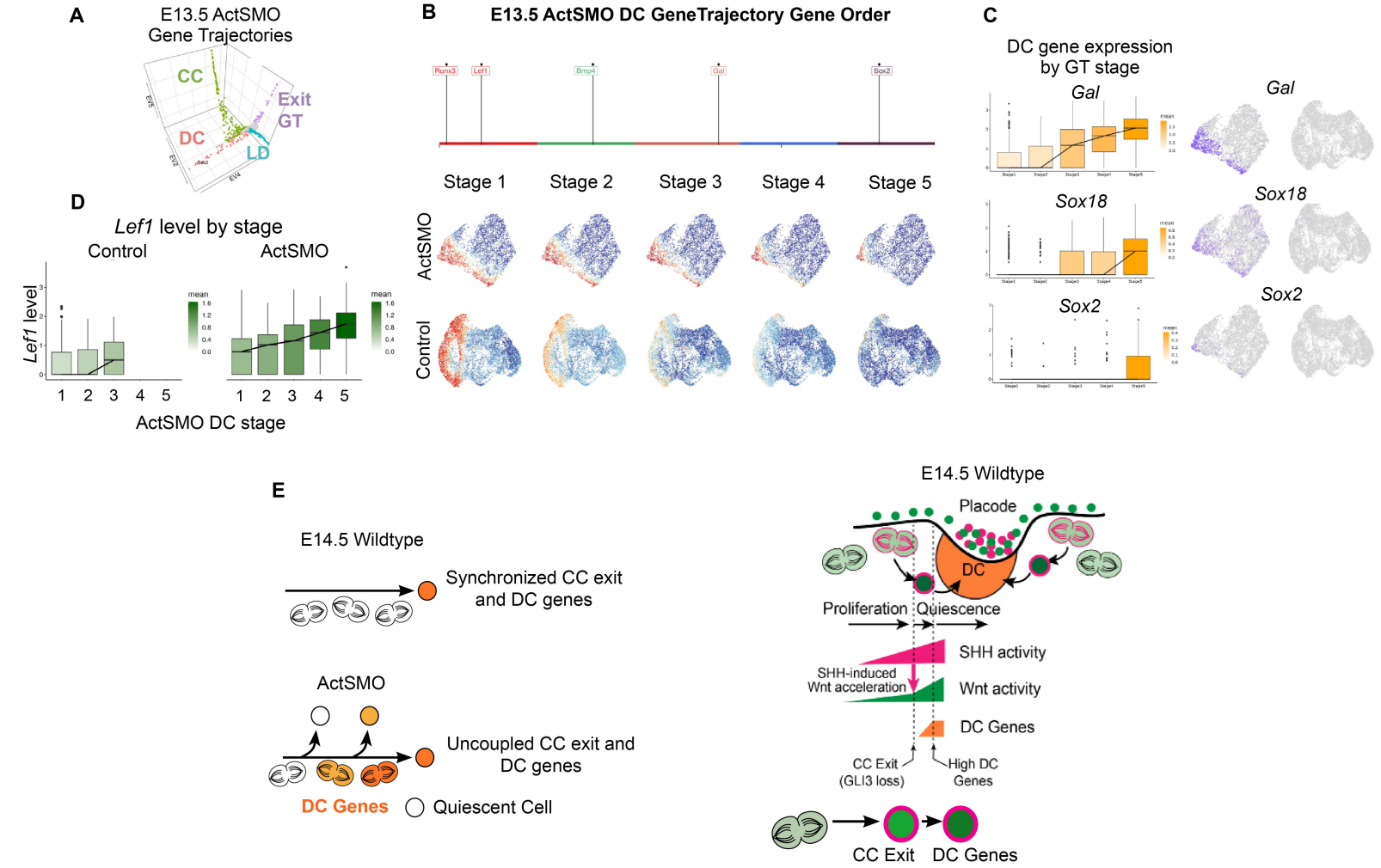
A
E13.5 ActSMO
Gene Trajectories
CC
Exit
GT
DC
LD
B
E13.5 ActSMO DC GeneTrajectory Gene Order
Runx3
Lef1
Bmp4
Gal
Sox2
Stage 1
Stage 2
Stage 3
Stage 4
Stage 5
ActSMO
Control
C
DC gene expression
by GT stage
Gal
Sox18
Sox2
D
Lef1 level by stage
Control
ActSMO
Lef1 level
mean
1 2 3 4 5
ActSMO DC stage
E
E14.5 Wildtype
Synchronized CC exit
and DC genes
ActSMO
Uncoupled CC exit and
DC genes
DC Genes
Quiescent Cell
E14.5 Wildtype
Placode
DC
Proliferation
Quiescence
SHH activity
SHH-induced
Wnt acceleration
Wnt activity
DC Genes
CC Exit
(GLI3 loss)
High DC
Genes
CC Exit
DC Genes

Figure 7

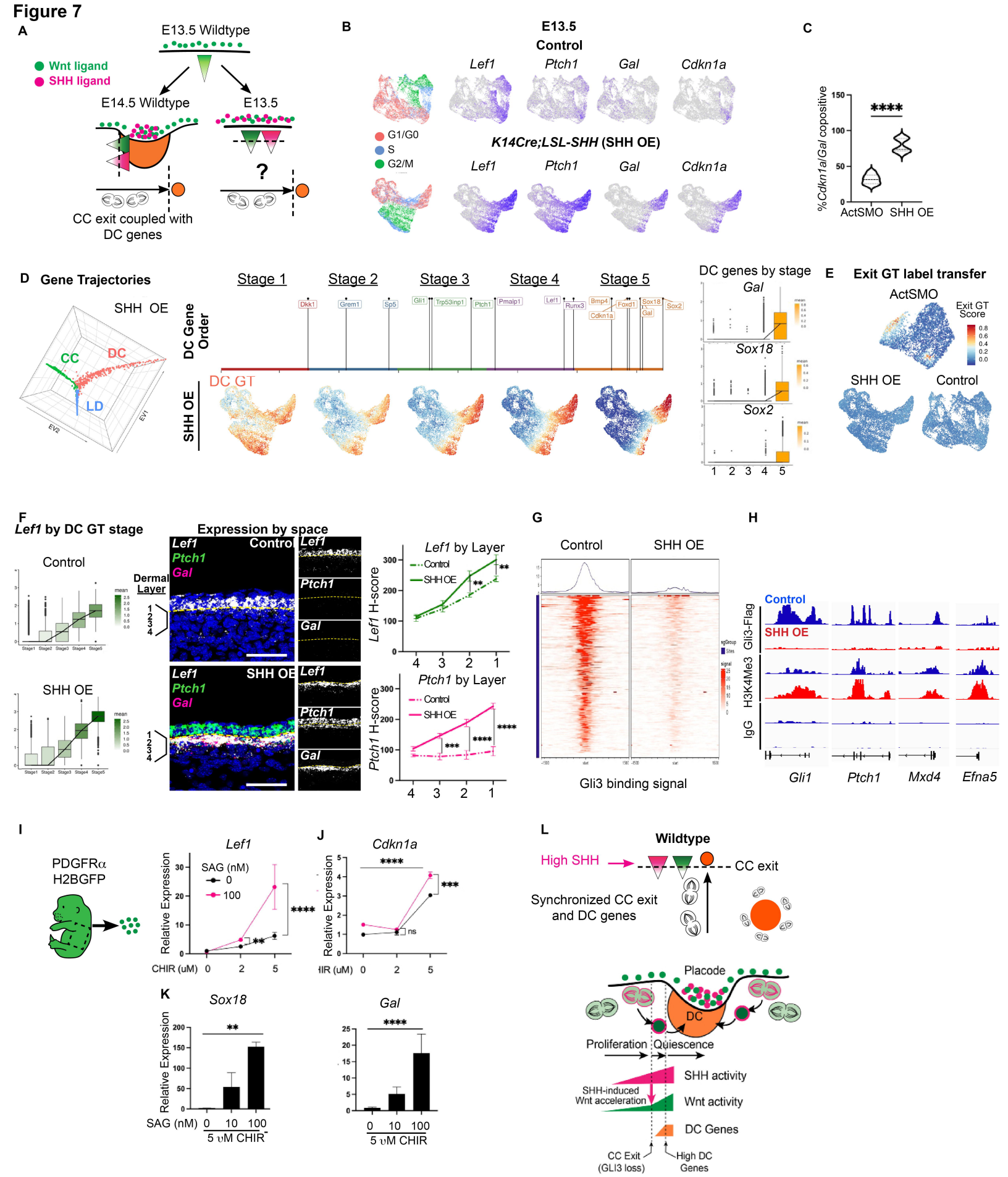
A
E13.5 Wildtype
Wnt ligand
SHH ligand
E14.5 Wildtype
E13.5
?
CC exit coupled with DC genes
B
E13.5
Control
Lef1
Ptch1
Gal
Cdkn1a
G1/G0
S
G2/M
K14Cre;LSL-SHH (SHH OE)
C
%Cdkn1a/Gal copositive
****
ActSMO
SHH OE
D
Gene Trajectories
SHH OE
CC
DC
LD
EV1
EV2
Stage 1
Stage 2
Stage 3
Stage 4
Stage 5
DC Gene Order
DC GT
SHH OE
DC genes by stage
Gal
Sox18
Sox2
E
Exit GT label transfer
ActSMO
Exit GT Score
SHH OE
Control
F
Lef1 by DC GT stage
Control
SHH OE
Expression by space
Lef1
Ptch1
Gal
Control
SHH OE
Dermal Layer
Lef1 by Layer
Ptch1 by Layer
Lef1 H-score
Ptch1 H-score
G
Control
SHH OE
Gli3 binding signal
H
Control
SHH OE
Gli3-Flag
H3K4Me3
IgG
Gli1
Ptch1
Mxd4
Efna5
I
PDGFRα
H2BGFP
Lef1
SAG (nM)
0
100
Relative Expression
CHIR (uM)
J
Cdkn1a
ns
K
Sox18
Gal
SAG (nM)
5 υM CHIR
L
Wildtype
High SHH
CC exit
Synchronized CC exit and DC genes
Placode
DC
Proliferation
Quiescence
SHH activity
SHH-induced Wnt acceleration
Wnt activity
DC Genes
CC Exit (GLI3 loss)
High DC Genes